

Oberlin College

Honors Thesis

**Separation of FeO and Fe₃O₄
Nanoparticles Using an Inverted
Linear Halbach Array**

Jason Heitler-Klevans

Department of Physics and Astronomy

March 31, 2017

Executive Summary

Separation of FeO and Fe₃O₄ Nanoparticles Using an Inverted Linear Halbach Array

By Jason Heitler-Klevans

Magnetic nanoparticles are tiny particles that act like little magnetic dipoles, but which behave significantly differently from larger magnets. When coated properly and suspended in a fluid such as water, these particles may be used for a variety of medical applications, including drug delivery, biological imaging, and cancer therapy. However, uniformity of size and magnetic properties is essential for the use of magnetic nanoparticles in any of these techniques. Precise and efficient separation and purification methods are therefore necessary for proper implementation of nanoparticles.

In this thesis, we study the novel use of an arrangement of magnets to separate out two types of nanoparticles from a suspension, one composed of magnetic Fe₃O₄, and the other composed of nearly non-magnetic FeO. When a fluid containing these particles is passed above the magnets, the more magnetic particles tend to sink towards the magnets, while the less magnetic particles pass through. This should allow us to separate the two types of particles from one another into two solutions in a controlled fashion.

We first explain the physics behind the separation process, and continue to describe the behavior of our specific nanoparticles suspended in fluid. Our experimentation explores the effect of concentration and field gradient on the separation and develops mathematical models to understand the outcomes. We conclude that our setup provides an adjustable method for nanoparticle separation and outline a method for evaluating the efficiency of the device, along with suggestions for future improvements in the process.

Acknowledgments

I would like to express my deepest gratitude to the following persons for their support during the production of this thesis.

Firstly, I would like to thank my advisor, Professor Yumi Ijiri, for her time, insight, and support throughout my time as her researcher and student. She has given so much time and energy to helping me grow, learn, and succeed, and I owe her so much. I would specifically like to thank her for welcoming me into her lab, and for encouraging me to be resourceful, diligent, and thorough.

Second, I would like to thank the faculty and researchers who have proven invaluable in this endeavor. My gratitude to Anna Samia and her student Eric Abenojar for their continued support in providing samples, data analysis, and information throughout this process. I would also like to thank Doug Feller for his many hours of assistance in machining countless sample holders over the years.

I would like to thank my girlfriend, Helen Kramer, for her love, support, and strategic use of chocolate to maintain my morale and energy. She has stayed a constant source of comfort and calm, and I cannot thank her enough. I would also like to thank my brother Ari Heitler-Klevans, for his willingness to listen to me as I thought through countless physics problems, and for his steady support throughout.

I would like to thank my friends and family, specifically my parents and grandparents, for their understanding, compassion, and affirmation. I could not have wished for a more wonderful group of people in my life. Thanks to my lab partners Emily Hamlin, Naiyuan Zhang, and Hillary Pan, and a special thanks to the other physics honors students Kinori Rosnow, Hannon Ayer, Ian Hunt-Isaak, Jacob Turner, Dahyeon Lee, and Kai Shinbrough for the many hours we have spent together earning this major.

Additional thanks to the NSF DMR-1606887 grant for providing funding for this project, along with the NSF DUE-9950606 which funded the VSM magnetometer used extensively in this thesis.

Contents

Executive Summary	i
Acknowledgments	ii
List of Figures	v
List of Tables	vii
Glossary and Physical Constants	viii
1 Introduction and Motivation	1
2 Background and Theory	6
2.1 Magnetism in Materials	6
2.2 Magnetic Separation Mechanisms	14
3 Experimental Procedures	18
3.1 Nanoparticle Synthesis	18
3.2 Structural Characterization	19
3.3 Magnetic Characterization	20
3.4 Procedures for Nanoparticle Separation	21
4 Results and Analysis	27
4.1 Initial Structural Characterization Results	27
4.2 Initial Magnetic Characterization Results	29
4.3 Separation Results	31
4.3.1 Separations with Varying Particle Concentrations	32
4.3.2 Separations with Varying Field Gradient	35
4.4 Receiver Operating Characteristic Analysis	39

5	Conclusion and Future Work	42
5.1	Conclusions	42
5.2	Future Work	43
A	Mathematica Code for VSM Analysis	49
B	Solidworks CAD Designs	58

List of Figures

2.1	Magnetic responses associated with different types of magnetic materials	8
2.2	Magnetic domains of ferromagnetic materials in the absence and presence of a saturating magnetic field	9
2.3	A moment-based picture of magnetic nanoparticles in the absence and presence of a saturating magnetic field	10
2.4	A plot of a normal distribution, a lognormal distribution, and a gamma distribution to demonstrate the differences between them .	13
2.5	A plot of potential ROC curves demonstrating the meaning of this form of analysis	17
3.1	Lakeshore 7307 Vibrating Sample Magnetometer at Oberlin College.	20
3.2	Diagrams of the Kel-F sample holders used for VSM measurements and machined by Doug Feller	21
3.3	The constructed linear Halbach array with 47 NdFeB permanent magnets held together by set screws and an aluminum frame . . .	22
3.4	Plot of the B field along the length of the array at four different distances from the array, as modeled by FEMMView	22
3.5	Plot of the field lines along the length of the array and the orientation of magnet magnetizations, as modeled by FEMMView . .	23
3.6	Picture of observable banding of magnetic Fe ₃ O ₄ nanoparticles when placed above the array	23
3.7	Array-channel assembly design with toluene-compatible glass channel	24
3.8	Schematic of separation at an optimal distance and one complication that could arise	26

4.1	TEM characterization of the particles received	28
4.2	XRD characterization of the particles received	28
4.3	Initial magnetometry results for FeO and Fe ₃ O ₄ suspensions	29
4.4	Magnetometry results confirming changes in particle moment by comparing liquid samples from the FeO particles taken a month apart	31
4.5	Initial magnetometry results for mixtures of FeO and Fe ₃ O ₄ with varying concentrations	32
4.6	Magnetometry results for the filtrate solutions from the separations performed on suspensions of varying concentration	34
4.7	Magnetometry results for the initial suspensions of FeO and Fe ₃ O ₄ mixtures separated at different field gradient	35
4.8	Pictures of the channel during separation for the separations performed at varying field gradients	37
4.9	Magnetometry results for the filtrate solutions from the separations performed on suspensions separated at varying field gradient	38
4.10	A plot of the signal shift from Fe ₃ O ₄ to FeO versus applied field gradient after separation	39
4.11	A plot of potential ROC curves with one point calculated from the 25/75 mixture of FeO/Fe ₃ O ₄	41
B.1	Design of plexiglass channel top for the toluene-compatible glass channel	58
B.2	Design of glass plate for the toluene-compatible glass channel	59
B.3	Design of stainless steel base plate for the toluene-compatible glass channel	60

List of Tables

2.1	The potential results of a binary sort presented in the context of ROC analysis	16
4.1	Magnetic characterization results for the initial FeO and Fe ₃ O ₄ samples using Langevin analysis and assuming a lognormal distribution of magnetic moments	30
4.2	Percentages of VSM signal attributed to the FeO and Fe ₃ O ₄ particles for mixtures of different concentrations, using a double Langevin analysis	33
4.3	Percentages of VSM signal attributed to the FeO and Fe ₃ O ₄ particles for initial mixtures used in the changing field gradient experiment, using a double Langevin analysis	36
4.4	Percentages of VSM signal attributed to the FeO and Fe ₃ O ₄ particles for the filtrates obtained by varying the field gradient, using a double Langevin analysis, and with percentage shifts from initial samples shown	38
4.5	Calculated values of the false positive fraction used in ROC analysis, as calculated from the results for the filtrates obtained by varying the field gradient	39

Glossary and Physical Constants

Boltzmann's Constant	k_b	=	1.38×10^{-23} J/K
Permeability of Vacuum	μ_0	=	$4\pi \times 10^{-7}$ N/A ² in SI or 1 in CGS
Avogadro's Constant	N_A	=	6.022×10^{23} mol ⁻¹
Room Temperature	T	=	298 K
Viscosity of Toluene	$\eta_{toluene}$	=	0.580 cP

Chapter 1

Introduction and Motivation

Ferrofluids are stable solutions that consist of magnetic particles with micron to nanometer diameters coated with a surfactant and suspended in a fluid. Ferrofluids were first developed in the 1960s, and have continued to be the subject of extensive research ever since (Franklin). The physical and magnetic properties of these nanoparticles allow for a wide range of applications including in industrial vacuum parts, memory storage, and wastewater remediation (Sigamaneni et al.). By far, one of the most attractive areas of application of ferrofluids is in biomedicine due to the alterability of a nanoparticle's surface and its specific magnetic behavior (Krishnan).

In particular, several important areas of research for nanoparticle use in biomedicine include targeted drug delivery, improved magnetic resonance imaging (MRI), and a form of cancer or tumor treatment called hyperthermia (Pankhurst et al.). Nanoparticles are small enough for insertion into the body and can pass through most layers of organic matter such as cell membranes. During and after synthesis, nanoparticles are coated with some form of surfactant in order to stabilize the particles in solution and may then be coated with a desired chemical, medicine, or marker. When placed inside a cell or area of the body, the magnetic nanoparticles may be manipulated to move precisely using external magnetic fields, such

that the exact nature of drug delivery may be more controlled (Williams et al. 1, Haefeli and Chastellian, Hayden and Haefeli). Additionally, ferrofluids can be used as a negative contrasting agent in an MRI scan, providing clearer imaging than commercially available materials (Malekzadeh et al.). Extensive research has investigated the creation of a new form of imaging technology called magnetic particle imaging (MPI). MPI allows for a quantitative spatial mapping of magnetic nanoparticles, enabling a flexible form of imaging with the potential for higher resolution than current medical diagnostic technologies (Samia 2013, Gehrcke). Magnetic nanoparticles also have the potential to aid in hyperthermia treatment, a method that primarily targets cancer or tumor cells. The particles are injected into the infection site, and then an alternating external magnetic field is used to transfer energy to the particles in the form of heat in order to either release heat-sensitive drugs into the tumor or to denature the desired cells (Ito et al.).

However, all biomedical applications of magnetic nanoparticles rely on uniformity of particle size and magnetic properties. Particles of different sizes and chemical compositions will exhibit different magnetic responses, and in ferrofluids, can then lead to a wider range of fluid response in the presence of an external magnetic field. The use of large macroscopic quantities of particles with different magnetic properties can have unintended and potentially toxic results on a body, making the use of such fluids unacceptable for medical practice. Unfortunately, while many synthesis methods may produce organic solutions of nanoparticles with high precision, the transfer of such particles to water introduces a number of potential changes in size, surface uniformity, and chemical composition, all of which may impact the magnetic properties of the particles. In addition, chemical variation within a nanoparticle can occur without a variation in particle size, resulting in very different magnetic behaviors.

Although there are many research groups focused on synthesizing nanoparticles, and there are ways to separate based on sizes such as through the use of mechanical sieves, very few approaches focus on separating based on magnetic effects. We will discuss several of the main methods to purify on the basis of magnetic properties here, including the use of high gradient magnetic separation (HGMS), field flow fractionation (FFF) methods, the differential magnetic catch-and-release (DMCR) technique, and low gradient magnetic separation (Stephens et al.).

Each of these techniques relies on the unique properties of magnetic nanoparticles in order to function. Magnetic nanoparticles used in biomedicine are typically superparamagnetic as discussed in Section 2.1; in the presence of a small external field, the particles respond readily and will tend to aggregate into chains of particles. This allows for greater discrimination in the process of separation, as smaller or less magnetic particles will have an exponentially smaller probability of chaining together. In addition, non-uniform fields (field gradients) will induce a magnetic force, drawing the aggregated particles towards the source of the external field, which can be as simple as a permanent magnet.

HGMS provides a relatively straight-forward approach by placing the ferrofluid in a container filled with susceptible wires and then activating an electromagnet nearby (Faraudo et al.). This generates a high-gradient field and causes rapid particle aggregation around the wires, which is ideal for collecting micron scale particles. Unfortunately, the method does not allow for more fine-tuned separation or purification of magnetic nanoparticle suspensions, as the size of the particles is insufficient for separation in this way.

The FFF methods provide more variety and finesse into magnetic separation than HGMS, and come in several forms such as magnetic field flow fractionation (MFFF), quadrupole magnetic field flow fractionation (QMgFFF), and cyclical electrical field flow fractionation (CyFFF). FFF techniques rely on the fact that fluid flowing near the walls of a capillary tunnel or channel tend to travel slower than those travelling in the middle of the channel (Stephens et al.). By flowing a polydisperse ferrofluid through such a channel and applying an external magnetic field, larger particles or particles with a higher magnetic moment tend to aggregate near the walls and flow slower than smaller or less magnetic moments. The different sizes of particles are then collected at different times from the outlet of the tube. Altering the setup by introducing a quadrupole magnet to achieve QMgFFF improved the efficiency of this method without drastically increasing the complexity or changing the separation method used (Carpino et al., Orita et al.). Additionally, the electromagnetic setup used to make the quadrupole allowed for programmable separation, increasing the flexibility of this method (Williams et al. 2). CyFFF takes another approach to the same method, wrapping a capillary tube around an electromagnet and causing larger particles to aggregate in the portion of the tube closest to the magnetic (Tasci et al.).

DMCR provides a slightly more nuanced method of separation, where the external magnetic field is now applied horizontally rather than vertically relative to the tubes containing the ferrofluid. By using a more rigorous approach involving a balance of drag and magnetic forces, this technique allows for more careful and precise separation of nanoparticles by size (Beveridge et al.).

The use of low-field separation methods reduces the setup complexity and cost of construction, and makes use of inter-particle interactions more explicitly. In a low-field environment, differences between large and small or magnetic and non-magnetic particles have a greater impact on typical particle behavior (Yavuz et al., Cuevas et al.). However, previous experimental setups have not allowed for comprehensive analysis or a quantitative understanding of the separation process in relation to theory.

While all of these techniques hold interest in the area of magnetic nanoparticle separation, none provide a clear basis for industrial use due to limits on sample sizes. For FFF methods, the constant flow of nanoparticle suspension suggests use in commercial separation of nanoparticles, but this technique requires slow flow rates and small sample sizes such as 20 μL of sample pumped at 0.1 mL/min (Carpino et al.). Current DMCR research still deals with limited sample sizes and is not easily scalable. Therefore, an alternative method for magnetic separation is clearly necessary that allows for both precision in separating nanoparticles and scalability for industrial or at least laboratory preparation purposes.

Our recent work employs a linear inverted Halbach array to achieve separation of magnetic nanoparticles of varying moments (Ijiri et al.). It is well known that a special arrangement of magnets called a Halbach array results in a non-symmetric magnetic field, with one high field side and one low field side. Designed in 1980 by Klaus Halbach, the array takes the form of a series of magnets with their magnetizations oriented in a rotating pattern (Halbach). While most research that employs a Halbach array uses the high field side, the inverted side provides a combination of low magnetic field and high field gradient. The field gradient enables the use of magnetic forces to draw particles towards the array, while the low field aspect allows for discrimination between higher and lower moment particles (Hoyos et al.). This approach has the advantage of allowing for precise control over

separation parameters such as field gradient, as well as a scalable design with the potential for larger sample sizes and industrial use.

Initial research has already demonstrated the ability of the array to discriminate between particles with different magnetic moments due to their particle size (Ijiri et al.). But while differences in size do often account for differences in magnetic moment, other factors such as chemical composition, surface effects, particle shape, and the surfactant coating may influence their magnetic behavior. We have yet to explicitly evaluate the magnetic separating capacity of the device or characterize its efficiency.

In this thesis, we investigate the separation of wüstite (FeO) and magnetite (Fe_3O_4) nanoparticles of similar size in order to further characterize the efficiency and effectiveness of the linear inverted Halbach array as a sorting mechanism. Chapter 2 outlines the theory behind magnetism in materials, describes the properties of superparamagnetic particles, provides a model and justification for our assumption of a distribution of magnetic moments, details the mechanics of magnetic separation, and outlines an analytical tool for quantifying the efficiency of our sorting mechanism. Chapter 3 provides details on our measurement procedures and experimental setup, and Chapter 4 describes the results of two series of separations, one performed on samples of varying concentrations and one performed on samples under varying field gradient. Chapter 5 summarizes our results, and comments on the potential for future research and investigation of the device.

Chapter 2

Background and Theory

This chapter presents a basic overview of the theory of magnetism in materials, focusing on the magnetic properties of superparamagnetic materials as applied to nanoparticles in Section 2.1. In Section 2.2, an explanation of the relevant separation mechanism implemented by the Halbach array is presented, as well as a description of the proposed method used to analyze the efficiency of the array as a sorting mechanism.

2.1 Magnetism in Materials

In order to understand the magnetic properties of superparamagnetic nanoparticles, we must start by summarizing the magnetic behavior of different forms of materials in the presence of magnetic fields (Cullity). Additional information on the magnetic properties of different materials can be found in (Gersten and Smith, Griffiths).

Magnetism in materials arises from the intrinsic magnetic dipole moment of electrons, which is a consequence of an electron's spin and orbital angular momentum. From the Pauli exclusion principle, we know that electrons in the same atomic orbital must have opposite spins and that their net angular momentum is zero, and therefore that the magnetic

moments of paired electrons will cancel each other out. When discussing magnetic materials, we consider only the magnetic contribution of unpaired electrons. The sum of the magnetic moments in a material divided by its volume is defined as its magnetization \mathbf{M} ,

$$\vec{M} = \frac{\sum \vec{m}}{V} \quad (2.1)$$

where \mathbf{m} is the magnetic moment contribution from each atom, and V is the volume of the material. The magnetization of a material is dependent on temperature and any external magnetic fields. It can be expressed in relation to the external field \mathbf{H} by,

$$\vec{M} = \chi \vec{H} \quad (2.2)$$

where χ is known as the magnetic susceptibility tensor of the material, which can sometimes reduce to a simple constant for isotropic materials. In addition, the magnetization is related to the more general concept of \mathbf{B} , the induced magnetic field or magnetic flux density,

$$\vec{B} = \mu_0 (\vec{M} + \vec{H}) \quad (2.3)$$

where μ_0 is the vacuum permeability constant. The differences between different types of materials can be clearly illustrated through the relationship between \mathbf{M} and \mathbf{H} , as depicted in Figure 2.1. The commonly discussed types of magnetism in materials are diamagnetism (DM), paramagnetism (PM), ferromagnetism (FM), and anti-ferromagnetism (AFM). Additionally, materials constructed on a small enough scale ($10^{-6} - 10^{-9}$ m) can exhibit superparamagnetism (SPM), with the \mathbf{M} vs \mathbf{H} response shown below in Figure 2.1 (D).

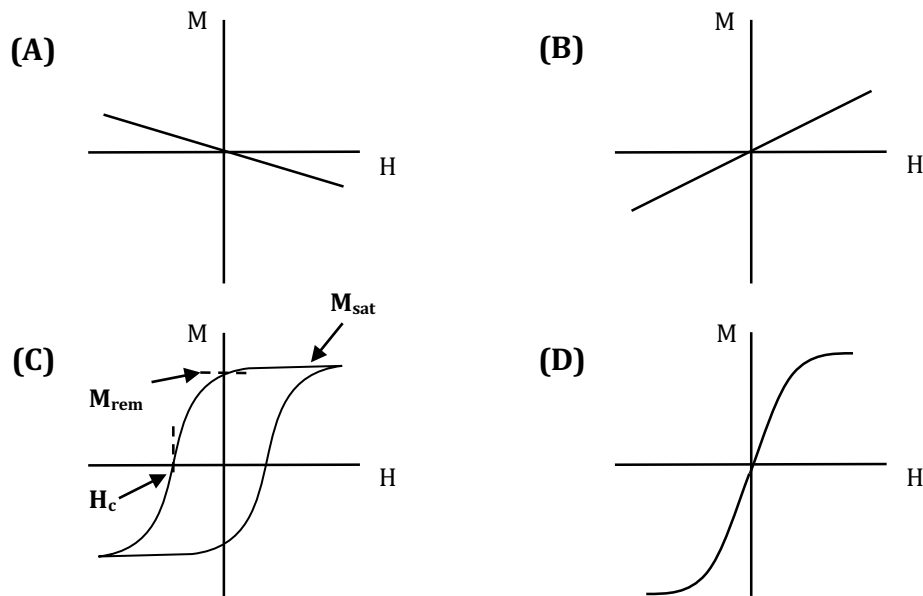


Figure 2.1: The \mathbf{M} vs \mathbf{H} field profiles for diamagnetic (A), paramagnetic (B), ferromagnetic (C), and superparamagnetic (D) materials. The coercivity (\mathbf{H}_c), the remanent magnetization (\mathbf{M}_{rem}), and the saturation magnetization (\mathbf{M}_{sat}) are indicated for the ferromagnetic graph.

Most stable substances are diamagnetic, containing primarily paired electrons, and their response weakly opposes the external magnetic field. Diamagnetic materials generally have a χ of -10^{-6} to -10^{-3} , whereas paramagnetic materials have a χ of 10^{-6} to 10^{-1} . Paramagnetic materials contain unpaired electrons that are sufficiently isolated from one another such that any external field will affect each magnetic moment individually, tending to align it with the field. In the absence of an external field, thermal energies are sufficient to align these magnetic moments randomly, resulting in a sample magnetization of zero.

Some materials contain enough unpaired electrons in close enough proximity that they retain a magnetization even in the absence of an external magnetic field. These substances, often known as permanent magnets and often ferromagnetic, have a magnetic response as illustrated in Figure 2.1 (C). In ferromagnetic materials, neighboring atomic magnetic moments interact and align parallel to one another, creating areas in the material called domains, as demonstrated in Figure 2.2 (A). Domains form in a manner that closes in their field lines in order to minimize the magnetostatic energy associated with the overall structure; otherwise, the large \mathbf{B} field generated by the aligned moments costs additional energy. In the absence of an external magnetic field, the domains may be oriented relatively

randomly, and the ferromagnetic material will have a net moment equal to the remanent magnetization, as indicated in Figure 2.1 (C) and Figure 2.2 (A). Note that the value is dependent on the history of the magnetic field treatment of the sample. The external field required to reduce the magnetization to zero is called the coercivity field H_c , and is also indicated in Figure 2.1 (C). The saturation magnetization is achieved when all of the domain moments are pointed in the direction of the applied field, as shown in Figure 2.1 (C) and Figure 2.2 (B).

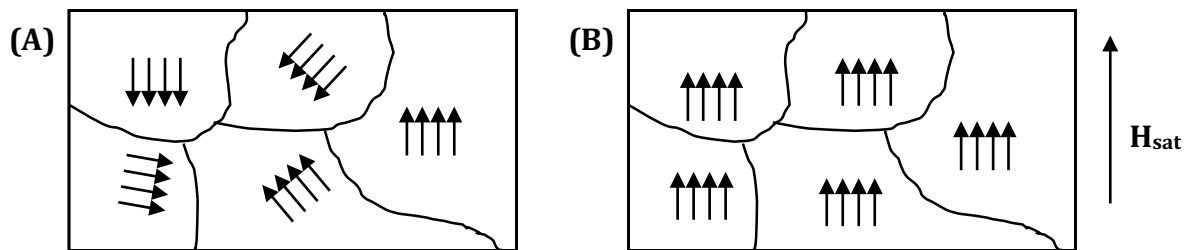


Figure 2.2: A naturally occurring ferromagnetic material with domains indicated (A), and that same material (B) in the presence of a saturating field upwards.

Antiferromagnetic materials consist of crystal structures containing planes of atoms with opposing magnetic moments relative to one another. Thus, otherwise magnetic materials such as FeO have a net magnetization of zero, with the magnetic moment of each plane canceling out those of its neighbors. We can therefore expect antiferromagnetic materials to have zero magnetization. However, irregularities in the crystal structure or surface effects may result in an imbalance of the opposing moments, with the effect of creating a weakly magnetic material. We will see this further in relation to the results in Chapter 4. In some materials, the magnetic moment contribution from alternating planes of atoms is not equal, leading to a net magnetization, in what is described as ferrimagnetism. In bulk, ferrimagnets such as Fe_3O_4 can appear to behave just like ferromagnets.

In the case of nanoparticles, another important type of magnetism to consider is superparamagnetism (SPM). On nano or micro-length scales, magnetic materials reach an energetic limit where a single magnetic domain is lower energy than multiple magnetic domains (Bean and Livingston). As previously stated, magnetic domains are formed in order to minimize magnetostatic energies, but in particles less than a characteristic size, the energy

to create domains is greater than the field energy inherent in a single domain. The particle will then act as one very large magnetic moment; its specific direction can be dictated by any preferred direction in the particle created through the crystal structure (crystalline anisotropy), shape (shape anisotropy), or surface (surface anisotropy), as well as the application of an applied magnetic field. These single-domain magnetic nanoparticles suspended in fluid result in a situation similar to that of paramagnetism, containing in effect a group of isolated magnetic moments as shown in Figure 2.3 (A). However, instead of single atomic moments as in paramagnetism, each moment is a result of a single magnetic domain that often contains 10^5 magnetic atoms, hence the name superparamagnetism. This leads to much larger values of χ than those associated with paramagnetic materials, as well as saturating fields achievable in the laboratory as depicted in Figure 2.3 (B).

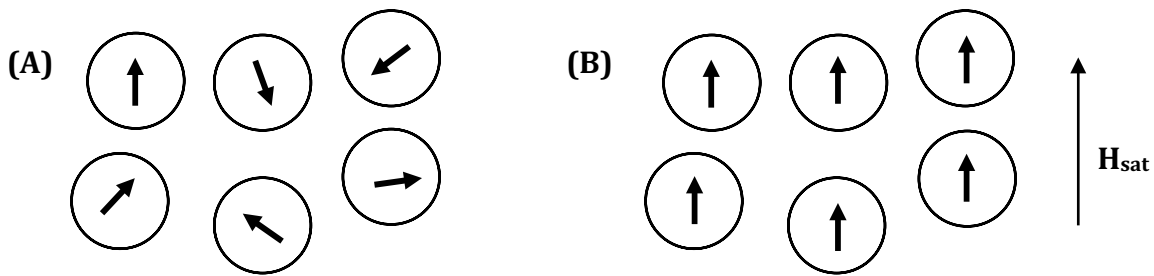


Figure 2.3: Nanoparticles suspended in fluid in the absence (A) and presence (B) of a saturating external magnetic field. The net magnetic moment of each particle is indicated with an arrow.

The superparamagnetic response of these particles to an applied magnetic field can be understood in terms of statistical mechanics from a discussion by (Bean and Livingston), ignoring any particle-particle interactions. For a particle of magnetic moment m in a direction θ relative to the external field \mathbf{H} , the particle's Zeeman energy will be given as $-mH \cos(\theta)$. For an assembly of such particles at temperature T , under the assumption of thermal equilibrium there will be a Boltzmann distribution of θ 's over the assembly. The net magnetization aligned in the direction of the external field is calculated by averaging $\cos(\theta)$ over the Boltzmann distribution. This results in the equation,

$$\bar{m} = \langle m \cos(\theta) \rangle = \frac{\int_0^\pi m \cos(\theta) e^{\frac{mH \cos(\theta)}{k_B T}} \sin(\theta) d\theta}{\int_0^\pi e^{\frac{mH \cos(\theta)}{k_B T}} \sin(\theta) d\theta} \quad (2.4)$$

where k_B is the Boltzmann constant and T is the temperature. This can be rewritten in terms of the ratio $\alpha = \frac{mH}{k_B T}$ and the substitution $x = \alpha \cos(\theta)$, such that Equation 2.4 becomes,

$$\bar{m} = \frac{m \int_{-\alpha}^{\alpha} x e^x dx}{\alpha \int_{-\alpha}^{\alpha} e^x dx} \quad (2.5)$$

The solution to this integral takes the form of

$$\bar{m} = mL(\alpha) = m \left[\coth(\alpha) - \frac{1}{\alpha} \right] = mN \left[\coth \left(\frac{mH}{k_B T} \right) - \frac{k_B T}{mH} \right] \quad (2.6)$$

where $L(\alpha)$ is known as the Langevin function and N is the total number of magnetic nanoparticles in the sample.

The Langevin function is commonly used to fit the magnetization versus applied field (**M** vs **H**) curve characteristic of a superparamagnetic sample, and allows us to extract relevant statistics by fitting the data. However, the single moment model is not always representative of an actual fluid sample due to variations in particle size and chemical composition, which may affect the magnetic moment. Several mathematical methods to model the particles in terms of a distribution of particle diameter or magnetic moment have been created in the past (Chen et al., Kakay et al., Chantrell), although some have more physical merit than others. For example, while a Gaussian curve provides the most straightforward form of modeling, it allows for non-physical negative values for diameter and particle moment. The Gaussian distribution is given by

$$p(x) = \frac{1}{\sqrt{2\pi\sigma^2}} e^{-\frac{(x-\mu)^2}{2\sigma^2}} \quad (2.7)$$

where μ is the median and σ is the standard deviation.

Previous research has focused on the use of a lognormal distribution or a gamma distribution for descriptions of nanoparticle diameter due to experimental evidence that

nanoparticle syntheses tend to lead to a skewed distribution of diameters. A comparison of these distributions was explored in the thesis of Jan-Philip Gehrcke, who demonstrated that the differences between these two distributions are minimal for the purposes of modeling magnetic nanoparticles as shown in Figure 2.4 (Gehrcke). Both distributions contain only positive values and may be adjusted easily, as compared with a Gaussian distribution of similar shape which contains non-physical negative values, as shown by the dotted green line in Figure 2.4. The gamma distribution is given as

$$p(x) = \frac{\beta^{-\alpha-1}}{\Gamma(1 + \alpha)} x^\alpha e^{-\frac{x}{\beta}} \quad (2.8)$$

where α is known as the shape parameter and β is known as the rate parameter. For research involving the time response of particles to an external field, the Gamma distribution provides more insight than the other probability functions. However, we have chosen to use the lognormal distribution due to its compatibility with our tools for analysis. The lognormal distribution is the natural logarithm of a Gaussian distribution as given by the equation

$$p(x) = \frac{1}{\sqrt{2\pi}\sigma x} e^{-\frac{(\ln x - \mu)^2}{2\sigma^2}} \quad (2.9)$$

where μ is the median and σ is the standard distribution for the corresponding Gaussian distribution. In previous research, a lognormal distribution in diameter for particles of constant magnetic moment m was assumed to account for any deviation in magnetic behavior (Ferguson et al., Chantrell). In this thesis, we consider particles that are effectively of the same diameter, but are composed of different materials, and therefore exhibit different magnetic moments based on variations in chemical composition or crystalline structure. In order to take all of these potential contributions into account, we assume that the particles follow a lognormal distribution of magnetic moment. From these considerations, we see that Equation 2.6 now takes the form of

$$\bar{m} = s \int_0^{\infty} p(m) \left[\coth \left(\frac{mH}{k_B T} \right) - \frac{k_B T}{mH} \right] dm \quad (2.10)$$

where s is a normalization factor and $p(m)$ is the lognormal distribution of magnetic moment in terms of the parameters μ and σ . An example comparison of this method is given in Appendix A, and for analysis, the limit of integration was changed from ∞ to 10^{-12} to improve the quality and decrease the computational time of analysis. This did not impact the fits obtained as the magnetic moments of the distribution were almost exclusively found to be values ranging from 10^{-18} to 10^{-14} emu. Additional terms were included in this equation, such as a slope term to account for the paramagnetic or diamagnetic contributions from the carrier fluid or sample holder respectively. An offset term was also used to account for any error in centering a sample relative to the measurement coils.

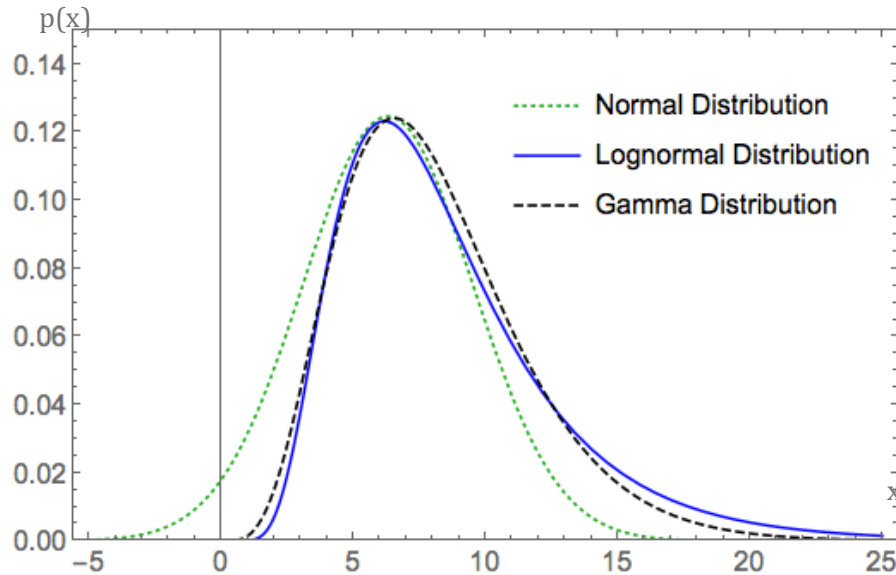


Figure 2.4: Shown is a comparison of the probability density functions $p(x)$ of a normal (dotted green line), a lognormal (solid blue line) and a gamma (dashed black line) distribution. As discussed, there are minimal differences in shape between the lognormal and gamma distributions.

During our experiments, we combined solutions of FeO and Fe₃O₄ nanoparticles to demonstrate separation processes for particles of different magnetic moments. In order to effectively model such solutions, we used an altered form of Equation 2.10, such that

$$\bar{m} = s_1 \int_0^\infty p_1(m) \left[\coth\left(\frac{mH}{k_B T}\right) - \frac{k_B T}{mH} \right] dm + s_2 \int_0^\infty p_2(m) \left[\coth\left(\frac{mH}{k_B T}\right) - \frac{k_B T}{mH} \right] dm \quad (2.11)$$

where $p_1(m)$ is described by the parameters μ_1 and σ_1 and $p_2(m)$ is described by the parameters μ_2 and σ_2 . We fit for $p_1(m)$ and $p_2(m)$ by testing the FeO and Fe₃O₄ particles individually and then fitting the data obtained from mixtures of these particles to find s_1 and s_2 . We then determined how much of the signal measured for a sample was attributed to the first distribution in comparison to the second. All of these aspects of our method for analysis are outlined in further detail in Appendix A.

2.2 Magnetic Separation Mechanisms

All of the separation methods described in Chapter 1 make use of the magnetic properties of the nanoparticles in order to discriminate between different magnetic particles in a colloidal suspension. From basic electromagnetic field theory, we know that the magnetic force upon an object is given by that object's magnetic moment and the magnetic field gradient, as expressed by,

$$\vec{F} = \nabla(\vec{m} \cdot \vec{B}) \quad (2.12)$$

where \mathbf{m} is the magnetic dipole moment and \mathbf{B} is the induced magnetic field (Griffiths). For a given field gradient, particles with different magnetic moments will experience different amounts of force in the direction of that gradient. However, the force experienced by individual particles is not great enough to induce particles to move in the direction of the magnetic gradient in time scales useful for experimentation (Williams and Poudel).

Fortunately, another effect comes into play in the form of interactions of magnetic nanoparticles with one another, an issue for example in a ferrofluid of sufficient particle concentration. Such a system has a potential energy associated with the magnetic dipolar coupling of nanoparticles, similar to that of electric dipoles (Van Reenan et al.). This dipole-dipole energy is given as,

$$U_{dd} = \frac{\pi\mu_0 M^2 d_m^6}{72(d_m + 2s)^3} \quad (2.13)$$

where U_{dd} is the dipole-dipole potential energy, \mathbf{M} is the particle magnetization, d_m is the magnetic diameter of the particle, and s is the depth of the non-magnetic surfactant used to suspend the particle in the solvent fluid. It should be noted that the magnetic diameter of the particle may be significantly different from the hydrodynamic diameter of the particle depending on the coating of the particle, and potentially the chemical composition of the particle. Given this energy, when a collection of particles experiences the magnetic force as described above, they may chain together. Therefore, m in Equation 2.12 is now the sum of the magnetic moments of the cluster of particles. In this way, particles that chain together experience a greater force than particles that do not, leading to an accelerated aggregation effect orders of magnitude greater than the magnetic force experienced by single particles. This could then allow for separation of particles based on chaining versus lack of chaining, although other issues must be considered.

One concern is the effect of Brownian motion, which counters the aggregation of particles. A simple calculation of the thermal energy $k_b T$ in comparison to the typical dipole-dipole energy for many magnetic nanoparticles shows that the two energies are of similar magnitude. We predict based on these opposing energies that for two particles with $U_{dd}/k_b T$ greater than 1, the particles will tend to chain together, and for $U_{dd}/k_b T$ less than 1 they will tend not to chain together.

In considering separation, we note that particles moving in a fluid are opposed by a drag force dependent on the fluid's viscosity and the size and speed of the particle. This relationship is given by Stoke's drag force for a fluid of viscosity η ,

$$\vec{F}_d = -3\pi\eta d_h \vec{v}_p \quad (2.14)$$

where d_h is the hydrodynamic diameter of the particle and v_p is the particle's velocity. This sets the timescale for separation to occur for characteristic clusters of some d_h .

In order to evaluate the efficiency of our separation method, we have begun to employ the Receiver Operator Characteristic (ROC) analysis, a practice commonly used to quantify the accuracy of a medical sorting process, such as a test of whether patients have a particular disease (Swets). For example, suppose a test indicates if a subject has malaria or not. For

any group of subjects, the test will indicate that a certain number are sick, and a certain number are healthy. Similarly, a magnetic nanoparticle sorting mechanism sorts out low magnetic moment particles from high magnetic moment particles based on whether they will chain together or not. We will call the portion of the sample where we expect the particles to go through the process without chaining the ‘Filtrate’, and the portion of the solution where we expect the particles to chain the ‘Residue’. This puts subjects into four categories, as demonstrated in the table below:

	Test Positive	Test Negative
Actually Positive	True Positive (tested sick and are sick) (low moment in the filtrate)	False Negative (tested healthy and are sick) (low moment in the residue)
Actually Negative	False Positive (tested sick and are healthy) (high moment in the filtrate)	True Negative (tested healthy and are healthy) (high moment in the residue)

Table 2.1: Given are the four possible categories of samples given a binary sorting mechanism. In parentheses are given what each category represents for the example of a medical test and for a sort of magnetic nanoparticles of varying magnetic moment (Swets).

The most commonly used relationships derived from these four categories are the sensitivity (the true positive fraction, TPF), and the specificity (which gives us the false positive fraction, FPF). The equations for these relations are given below:

$$Sensitivity(TPF) = \frac{TP}{TP + FN} = \frac{Filtrate_{low}}{Filtrate_{low} + Residue_{low}} \quad (2.15)$$

$$Specificity = \frac{TN}{TN + FP} = \frac{Residue_{high}}{Residue_{high} + Filtrate_{high}} \quad (2.16)$$

$$FPF = 1 - Specificity \quad (2.17)$$

We can graph TPF vs FPF to demonstrate what are known as ROC curves, as shown in Figure 2.5 to the right, where several example curves are depicted. A point along the diagonal dashed line (TPF = FPF) would indicate that for a random mix of particles the process would have no special discrimination between the two distributions of particles. The point in the upper left corner (TPF = 1, FPF = 0) would indicate a test with complete discrimination. ROC curves that lie closer to this point (like the red curve) demonstrate more efficient sorting processes than those with ROC curves closer to the diagonal (like the green one).

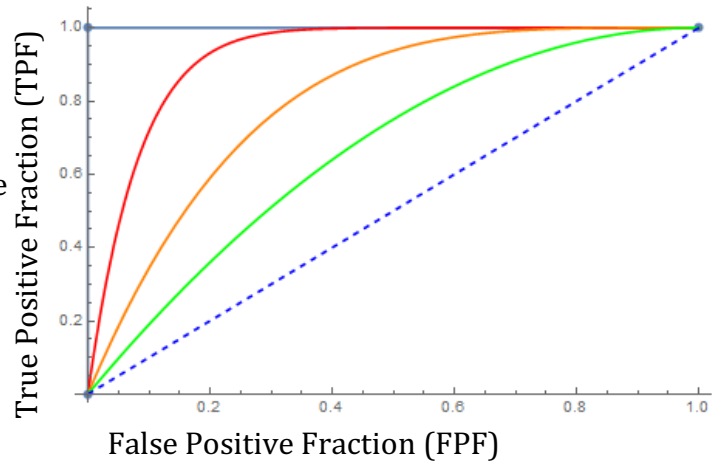


Figure 2.5: Example ROC Curves going from no discrimination (dashed) to complete discrimination.

By comparing the magnetic properties, chemical composition, and particle concentration, we can employ ROC curve analysis to quantify the efficiency of our sorting mechanism in discriminating between two types of particles, one composed of antiferromagnetic FeO, and one composed of ferromagnetic Fe₃O₄. Separations run with different parameters should lie at different points along such a curve, allowing us to quantify the sorting mechanism of a device by fitting the results of a series of separations based on changing separation parameters. We will discuss how the experiments that we performed could be used to construct an ROC curve in Section 4.4.

Chapter 3

Experimental Procedures

This chapter outlines the experimental procedures used for nanoparticle preparation, structural and magnetic characterization, and separation via the linear inverted Halbach array.

3.1 Nanoparticle Synthesis

All nanoparticle solutions used in this experiment were obtained from Professor Anna Samia and her students at Case Western Reserve University (CWRU). Wüstite (FeO) and magnetite (Fe₃O₄) magnetic nanoparticles were synthesized using a related process (Samia 2016). An oleate iron precursor was created by combining iron (III) chloride hexahydrate (FeCl₃•6H₂O) with sodium oleate and a solvent composed of deionized water, ethanol, and hexane, refluxing the mixture for 4 hours. The organic layer of that mixture was decanted for washing to remove byproducts, followed by drying under a vacuum for 72 hours. A solution of the iron oleate, oleic acid, and 1-octadecene was mixed under argon, heated to 100° C for 1 hour, and then refluxed at 320° C for another hour. The resulting FeO nanoparticles were precipitated out by centrifugation using an ethanol/toluene solvent.

Some of these FeO nanoparticles were converted to Fe₃O₄ by adding trimethylamine N-oxide [(CH₃)₃NO], heating at 130° C for 1 hour, and then heating to 280° C for another hour. The resulting Fe₃O₄ nanoparticles were extracted from the solution by centrifugation using an ethanol/toluene solvent. The particles were all transferred to toluene solutions and were diluted with anhydrous toluene in an argon glovebox, such that the solutions of FeO and Fe₃O₄ nanoparticles had the same particle concentration. Desired proportions of particles were thereafter achieved by mixing corresponding proportions of solution, such that a 50/50 mixture of FeO and Fe₃O₄ particles was obtained by mixing 1 part FeO solution with 1 part Fe₃O₄ solution. To prevent any additional oxidization of the FeO particles and to limit any degradation of the samples, the suspensions were kept in the argon-filled glovebox and filled with argon until separation. Additionally, after separation all of the collected suspensions were placed in argon-filled containers and stored in a fridge at 5° C.

3.2 Structural Characterization

Structural characterizations of the particles pre- and post-separation were conducted at CWRU in order to determine particle size, chemical composition, and concentration in solution; Transmission Electron Microscopy (TEM), X-Ray Diffraction (XRD), and Atomic Absorption Spectroscopy (AAS) were the three principal methods used.

TEM measurements were performed using an FEI Tecnai G2 Spirit BioTWIN transmission electron microscope operating at 120 kV to image particles dropped on a grid, and the imaging software ImageJ was used to analyze the data and calculate the average particle diameter (Samia 2016). Additionally, TEM images allowed for qualitative assessment of the particles, including information about the shape of the particles and surfactant coating. The crystalline composition of the particles was determined through XRD measurements, which were performed using a Rigaku MiniFlex X-ray powder diffractometer with Cu-K α radiation $\lambda=1.54$ Å. Dried and powdered samples of the nanoparticles were scanned for 2θ values of 25 to 65°. The total iron concentration for each liquid sample was determined using AAS measurements, which were performed using a fast sequential atomic

absorption spectrometer Varian 220FS AA to determine the concentration of iron in each sample.

The particle concentration of each solution was calculated using the TEM and AAS data, along with the known densities of FeO and Fe₃O₄.

3.3 Magnetic Characterization

A Lakeshore 7307 Vibrating Sample Magnetometer was used to determine the moment vs field profile of the samples before and after separations, and special sample holders were used to contain the liquid samples. All data were taken at room temperature for field values ranging from 0 to 1 T. A picture of the machine used is presented in Figure 3.1. The data were then fit to a Langevin function as explained in Chapter 2 with the assumption that the magnetic moments of the particles in each solution fit into a lognormal distribution, as explained in Appendix A. For solutions composed of a mixture of two types of particles, a double Langevin lognormal distribution of magnetic moment was used.

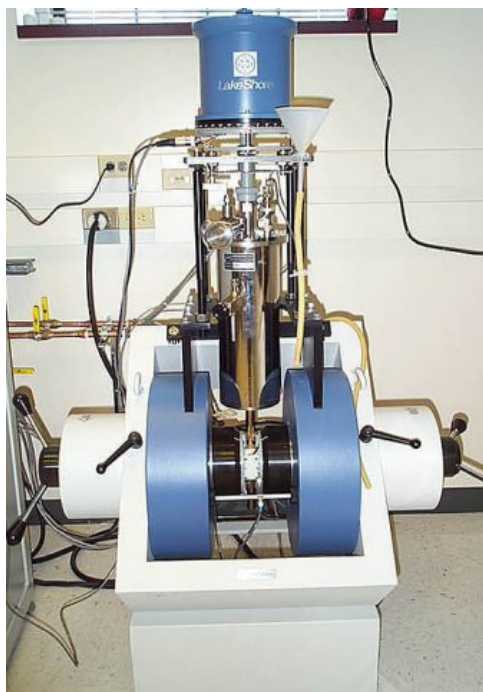


Figure 3.1: The Lakeshore 7307 Vibrating Sample Magnetometer at Oberlin College provided for by NSF DUE-9950606.

Sample holders were constructed in Oberlin College's machine shop from the material Kel-F (polychlorotrifluoroethylene), a clear elastopolymer. Kel-F is easily machinable, does not react in the presence of toluene, and most importantly has a diamagnetic signal in the μemu range, which is an order of magnitude less than most samples measured in the VSM. The design of the standard liquid sample holder used is outlined in Figure 3.2 (A, B), and each holder was filled with 50 μL of sample using a micropipettor and sealed with teflon tape. However, due to the low magnetic moment of the FeO nanoparticles, for some of the samples, the magnetic signal from the regular sample holder was still large enough to influence the VSM signal. To account for this, new sample holders, as outlined in Figure 3.2 (C) were machined such that the magnetic signal from the Kel-F above the sample would balance that from below the sample, effectively negating the holder's signal relative to the induction coils.

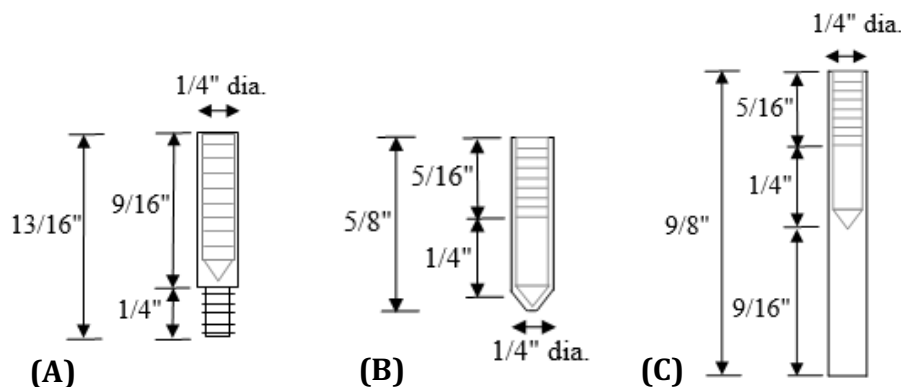


Figure 3.2: The sample holder top (A), standard bottom (B), and special bottom (C) machined at Oberlin College by Doug Feller. The standard sample holder consisted of parts A and B.

3.4 Procedures for Nanoparticle Separation

The inverted linear Halbach array used in this experiment was constructed of a series of Neodymium-Iron-Boride permanent magnets held with a set of screws in an aluminum case, as shown in Figure 3.3 (Poudel). The magnets were arranged such that the magnetization of each magnet was rotated 90° relative to the preceding magnet. The magnetic field and field gradient above the array were calculated using FEMMview software (Meeker), and the field profile for the low-flux side of the array is shown in Figure 3.4, with

the field profile verified using a Lakeshore gaussmeter probe. The field lines are depicted in Figure 3.5 as given by the FEMMview program. The average field and field gradient values for different heights above the array were calculated for use in separations.

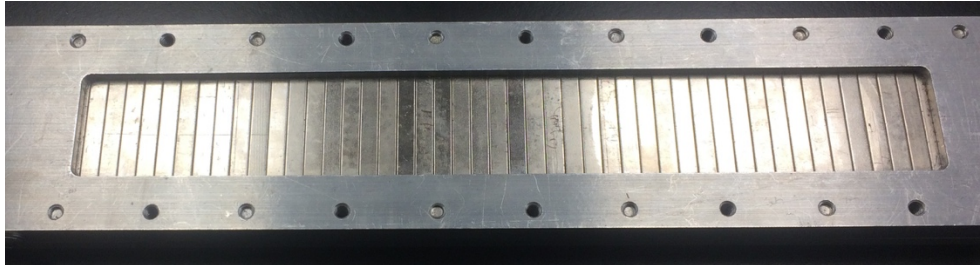


Figure 3.3: The inverted linear Halbach array used in this thesis, constructed of 47 NdFeB permanent magnets cased in aluminum.

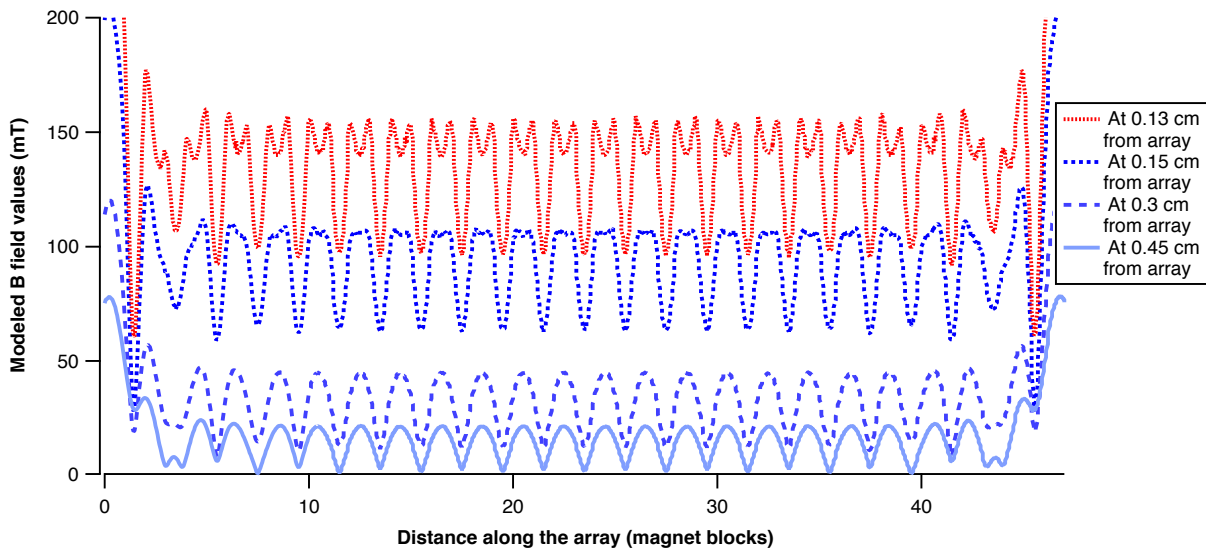


Figure 3.4: A plot of the B field along the length of the array measured at four heights above the array as modeled using FEMMView (Poudel).

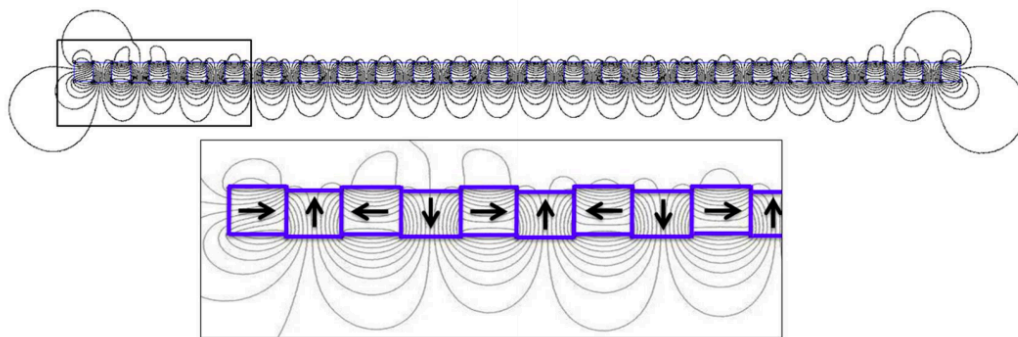


Figure 3.5: A diagram of the field lines created by the linear Halbach array and a magnified depiction from the grey boxed section, with the magnetizations of individual magnets indicated by black arrows (Poudel).

The liquid channel used in this experiment was constructed to allow fluid flow horizontally across the length of the array and was offset vertically from the array using two Standa 092354 stages. The vertical stages were zeroed relative to the array before each separation. The channel was constructed of a metal base plate, a Viton A gasket, a glass plate, and a plexiglass plate, with plastic tubing allowing for fluid to pass through. The Viton A gasket and glass plate were used due to their resistance to toluene. These materials fit together in a manner demonstrated in Figure 3.7, and are held together by using a set of screws and nuts. More details on the construction of the channel are given in Appendix B. Mineral oil was used to create a uniform index of refraction between the glass and the plexiglass, so that qualitative observations could be made about the particle activity in the channel.

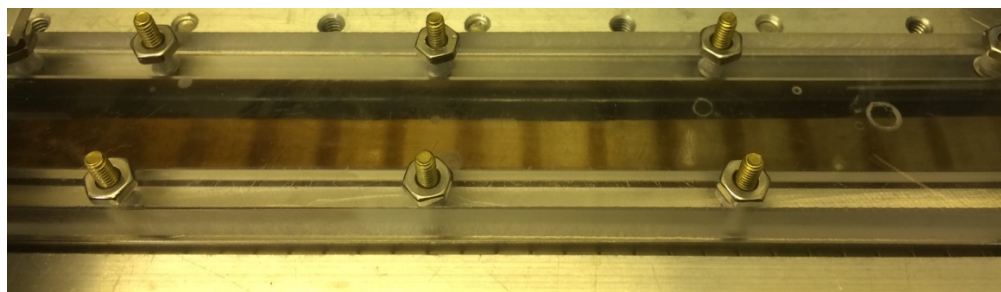


Figure 3.6: The toluene-compatible glass channel on top of the Halbach array during a separation. Distinct aggregation of the particles at specific points along the array is indicated by dark bands.

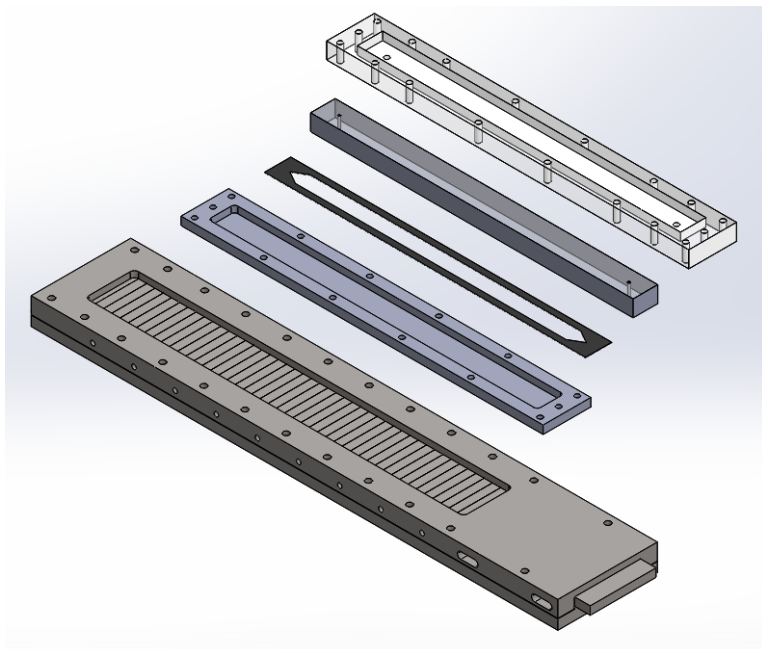


Figure 3.7: Array-channel design with toluene-compatible glass and Plexiglass channel

During the construction of the channel, the screws were tightened with a torque meter to avoid excess stress to the glass plate and to provide constant pressure on the gasket in order to create a liquid-tight seal. The inner 12 screws were tightened to a uniform maximum torque of 2.5 inch pounds, and the outer 6 screws were tightened to a uniform maximum torque of 1.5 inch pounds. After construction, the channel was filled with toluene to check for leaks and prepare the channel for each nanoparticle separation. All fluids were pumped into the channel using a Harvard Apparatus Syringe pump 11 Elite.

The prepared channel was filled with nanoparticle suspension and was then placed over the array. More nanoparticle suspension was pumped at a chosen pump rate and the channel was raised vertically over the array at a chosen height. The first 120 μL of suspension was separated to avoid obtaining particles that did not experience the magnetic force from the array. All the remaining fluid was collected in small vials. The fluid collected while the nanoparticle suspension was pumping at the chosen pump rate was dubbed the “filtrate.” Toluene was then pumped at the chosen pump rate, and the nanoparticle suspension obtained was dubbed the “intermediate” separation. The channel was removed from the array and the remaining suspension was pumped out at a high pump rate and dubbed the

“residue.” A diagram of the expected particle behavior during each separation is given in Figure 3.8.

In preparation for the separations performed with varying particle concentrations, five suspensions were created by combining samples of FeO and Fe₃O₄, such that there was one suspension each of 100% FeO, 75% FeO and 25% Fe₃O₄, 50% FeO and 50% Fe₃O₄, 25% FeO and 75% Fe₃O₄, and 100% Fe₃O₄, with percentages based on particle number. All five separations were run with the same parameters of height above the Halbach array and pump rate through the channel. The height of the channel was chosen to be 6.04 mm above the array, such that the particles would experience a 2.7 T/m field gradient. The separations were run with a pump rate of 15.3 μL/min based on the estimated time it would take a group of three Fe₃O₄ particles of median magnetic moment to sink to the bottom of the channel.

In preparation for the separations performed at varying field gradients, four suspensions were created such that each was composed of 50% FeO nanoparticles and 50% Fe₃O₄ nanoparticles. The separations were run at 5.08 mm, 4.13 mm, 3.18 mm, and 2.22 mm above the array, which corresponded to field gradients of 4.7 T/m, 10.6 T/m, 23.2 T/m, and 48.1 T/m respectively. These average field gradients were calculated from the FEMMView model shown in Figure 3.4 (Poudel). The pump rate for each separation was based on the estimated time it would take a group of three Fe₃O₄ particles of high magnetic moment (90th percentile) to sink to the bottom of the channel. Using this model, the pump rate increased with the field gradient due to the related increase of the magnetic force as given by equation 2.12. This higher pump rate was used based off of observations made in Section 4.3.1, and will be discussed in more detail in Section 4.3.2.

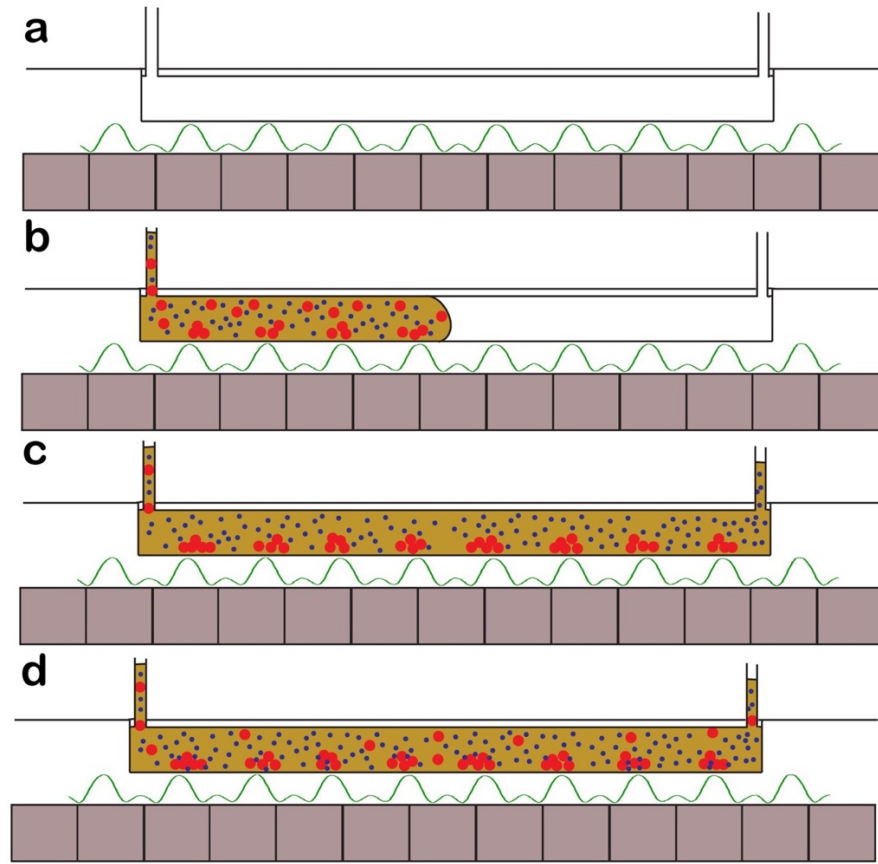


Figure 3.8: A schematic of the separation process at an optimal distance above the array, along with potential complications that could arise. (a) shows a depiction of the channel placed at an optimal distance above the array, (b) shows suspension being pumped into the channel, and (c) shows the ideal behavior of the suspension during separation. Here the larger red dots denote particles of higher magnetic moment (Fe_3O_4), and the smaller blue dots represent particles of lower magnetic moment (FeO). (d) shows a possible complication that could arise, with some high moment particles flowing through the channel unimpeded and some low moment particles aggregating to the bottom of the channel (Poudel).

Chapter 4

Results and Analysis

The results from structural and magnetic characterizations of magnetic nanoparticle suspensions and results of separation experiments are presented and interpreted here in sections 4.1 – 4.3. In section 4.4, the use of receiver operating characteristic analysis in the quantification of the efficiency of our sorting mechanism is discussed.

4.1 Initial Structural Characterization Results

Figure 4.1 shows typical transmission electron microscopy images taken by collaborators at CWRU. From the analysis software ImageJ, the FeO nanoparticles were found to have a diameter of 22.0 ± 1.4 nm, and the Fe₃O₄ nanoparticles were found to have a diameter of 22.2 ± 1.4 nm. The diameter of 22 nm was used in all analysis for these two samples, as the diameter of the Fe₃O₄ particles are well within the standard deviation of the diameter of the FeO particles. An additional sample of Fe₃O₄ nanoparticles was used for experimentation into gradient effects, and these particles were found to have a diameter of 16.76 ± 0.90 nm.

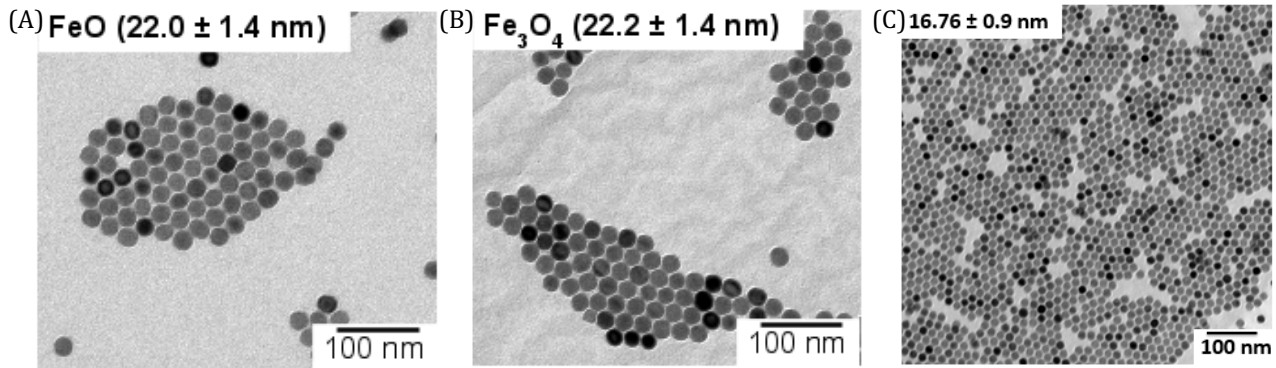


Figure 4.1: The TEM image of the FeO (A), the larger Fe₃O₄ (B), and the smaller Fe₃O₄ (C) nanoparticles, with the measured diameters 22.0 ± 1.4 nm, 22.2 ± 1.4 nm, and 16.76 ± 0.90 nm respectively.

From the X-ray diffraction results presented in Figure 4.2, the FeO nanoparticles were determined to be 94% FeO and 6% Fe₃O₄, the larger Fe₃O₄ nanoparticles were determined to be 8% FeO and 92% Fe₃O₄, and the smaller Fe₃O₄ nanoparticles were determined to be 6% FeO and 94% Fe₃O₄.

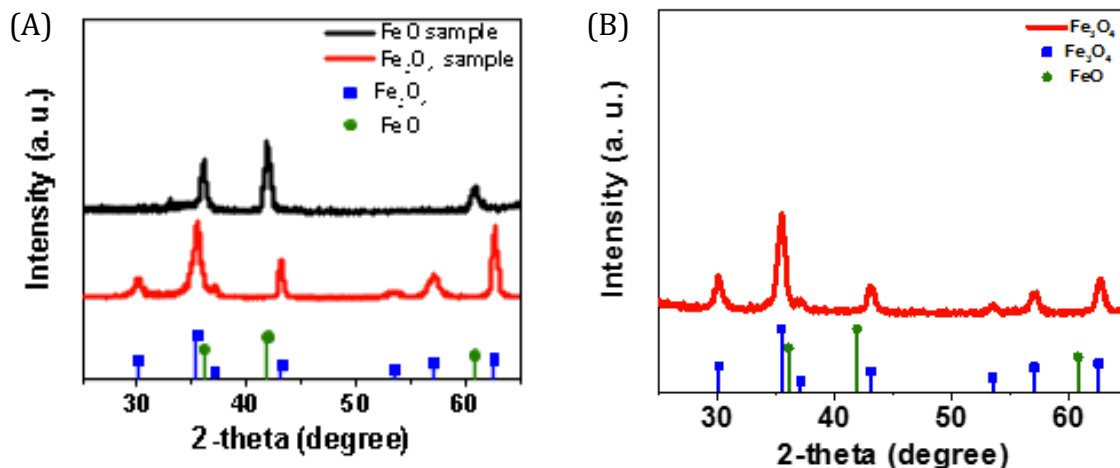


Figure 4.2: XRD spectra for the FeO and larger Fe₃O₄ nanoparticles (A) and for the smaller Fe₃O₄ nanoparticles (B). The points on the bottom of each figure indicate expected peak locations and relative intensities.

Atomic Absorption Spectroscopy analysis indicated that the FeO sample had an initial Fe concentration of 21.1 mg/mL, that the larger Fe₃O₄ sample had an initial concentration of 16.5 mg/mL, and that the smaller Fe₃O₄ sample had an initial concentration of 15.7 mg/mL. All the samples were diluted such that each had a particle concentration of approximately 2×10^{15} particles/mL.

4.2 Initial Magnetic Characterization Results

Vibrating Sample Magnetometry measurements were performed on each sample as is, with the field profiles shown below in Figure 4.3. The Fe_3O_4 measurements were performed on two separate samples, with average nanoparticle diameters of either 22 or 17 nm, as indicated by TEM analysis; the data are consistent with the expected Langevin signal for superparamagnetic nanoparticles of slightly different sizes. Two fluid samples were also taken from the FeO solution, one from before the experimentation began and the other a month later; unfortunately, the differences in the signals of these samples indicate that changes have taken place in the original FeO suspension over time.

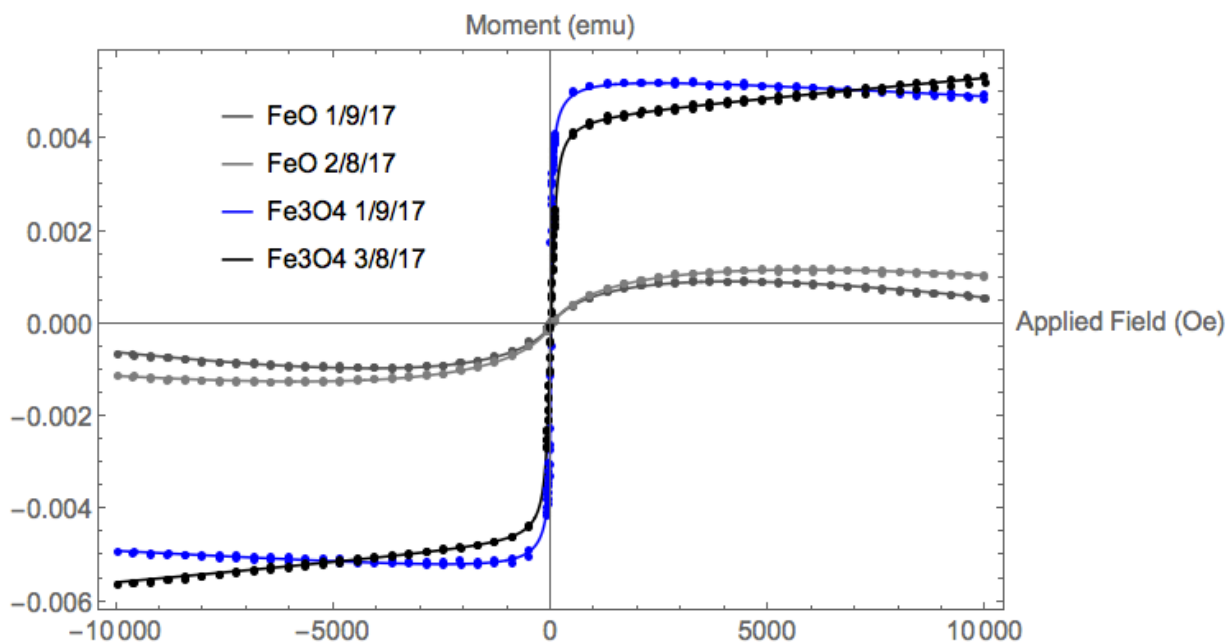


Figure 4.3: The VSM data (dots) and fit curves (lines) for the FeO and Fe_3O_4 samples, with the FeO samples being the same size and the Fe_3O_4 samples being of different sizes, corresponding to the labels used in Table 4.1. The slopes are the results of paramagnetic or diamagnetic contributions to the sample from the toluene solution or the sample holder respectively.

The moment versus field curves in Figure 4.3 were fit via the single Langevin lognormal moment distribution (SLLMD) analysis, with results given in Table 4.1, further confirming the qualitative observations just described. As discussed in Chapter 2, the natural

logarithm of μ value is equal to the median of the lognormal distribution, while the σ value indicates the standard deviation of the lognormal distribution. The median magnetic moment can therefore be calculated from the value of μ , while the relative size of each distribution can be interpreted by comparing σ values for different samples.

Sample	μ value	σ value	Low Moment (20 th percentile)	Median Moment (50 th percentile)	High Moment (90 th percentile)
FeO (1/9/17)	-39.2	1.8	2.0×10^{-18} emu	9.9×10^{-18} emu	1.1×10^{-16} emu
FeO (2/8/17)	-38.9	1.7	2.8×10^{-18} emu	1.3×10^{-17} emu	1.4×10^{-16} emu
Fe ₃ O ₄ (1/9/17)	-33.3	1.9	7.0×10^{-16} emu	3.4×10^{-15} emu	4.0×10^{-14} emu
Fe ₃ O ₄ (3/8/17)	-34.7	0.2	7.6×10^{-16} emu	8.6×10^{-16} emu	1.1×10^{-15} emu

Table 4.1: The fit values for the lognormal distribution (as defined by μ and σ) are presented, as well as the magnetic particle moments corresponding to different percentiles of the distribution. The samples are labeled by chemical composition and date measured. The two FeO samples are composed of particles of the same size (22.0 nm), while the two Fe₃O₄ have different average diameters (22.2 nm and 16.8 nm respectively).

The differences between the μ and σ values for the two different Fe₃O₄ samples can be attributed to the difference in diameter and the associated variation of diameter between the two. The smaller particles have a smaller moment per particle, and the smaller distribution of sizes corresponds with a smaller distribution of magnetic moments. As seen in Table 4.1, the later (2/8/17) data on the FeO particles resulted in a higher median moment, as well as a slight change in the standard deviation of the distribution relative to the earlier (1/9/17) data. Such changes must be taken into consideration during data analysis and imply that the particles may have a limited lifetime of utility. This issue is apparent in Section 4.3.2, particularly in Figure 4.7 and is discussed further in that section.

To ensure that the observed differences over time resulted from a change in the sample rather than some error associated with the VSM, several tests for reproducibility of signal were performed. A comparison of two data runs of the FeO sampled on 02/08/17 and one from the FeO sampled on 01/09/17 is shown in Figure 4.4. As indicated by the figure,

the differences between the VSM data acquired from the same sample are minimal compared with the VSM data acquired from the two different samples.

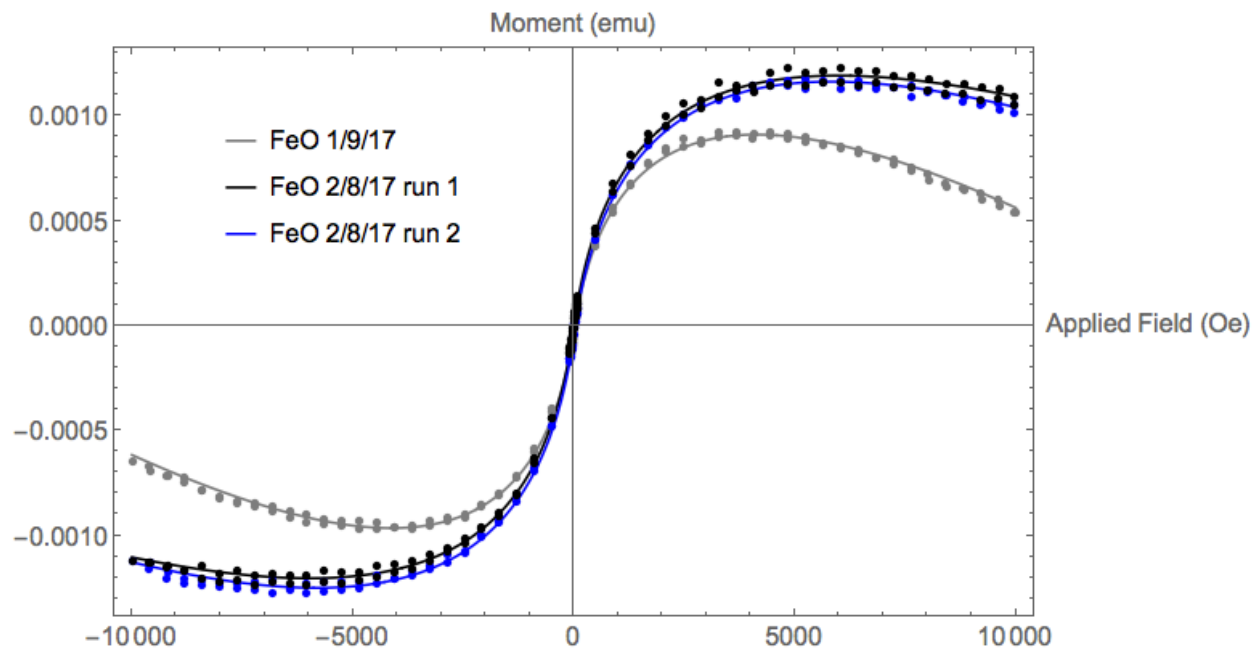


Figure 4.4: The VSM data (dots) and fit curves (lines) for the FeO sample, with one sample taken from the original solution in January and the other sample taken from the original solution in February. Two data runs from the second sample are displayed to indicate the reproducibility of the VSM data for individual samples as compared to the differences between samples.

4.3 Separation Results

As described in the Chapter 3, two series of separations were performed, one of varying concentrations of FeO and Fe₃O₄ particles at a single field gradient, and one of a 50/50 mixture of FeO and Fe₃O₄ particles at different field gradients. The larger Fe₃O₄ particles were used in the separations of varying concentration and the smaller Fe₃O₄ particles were used in the separations of varying field gradient, with results as described below in Section 4.3.1 and 4.3.2.

4.3.1 Separations with Varying Particle Concentrations

Initial VSM measurements of the suspensions of FeO and Fe₃O₄ with different concentrations were taken as shown in Figure 4.5. The data were fit using the double Langevin lognormal moment distribution (DLLMD) analysis as described in equation 2.11 with extracted information listed in Table 4.2. The percentages of VSM signal were determined by dividing the scale factor associated with each distribution by the sum of the scale factors ($s_1 + s_2$), as outlined in detail in Appendix A. As indicated by the information found in Table 4.2, the percentages of VSM signal change vary with the changes in concentration, with the Fe₃O₄ particles' signals dominating the shape of VSM data due to their vastly greater moment values as compared to the FeO particles.

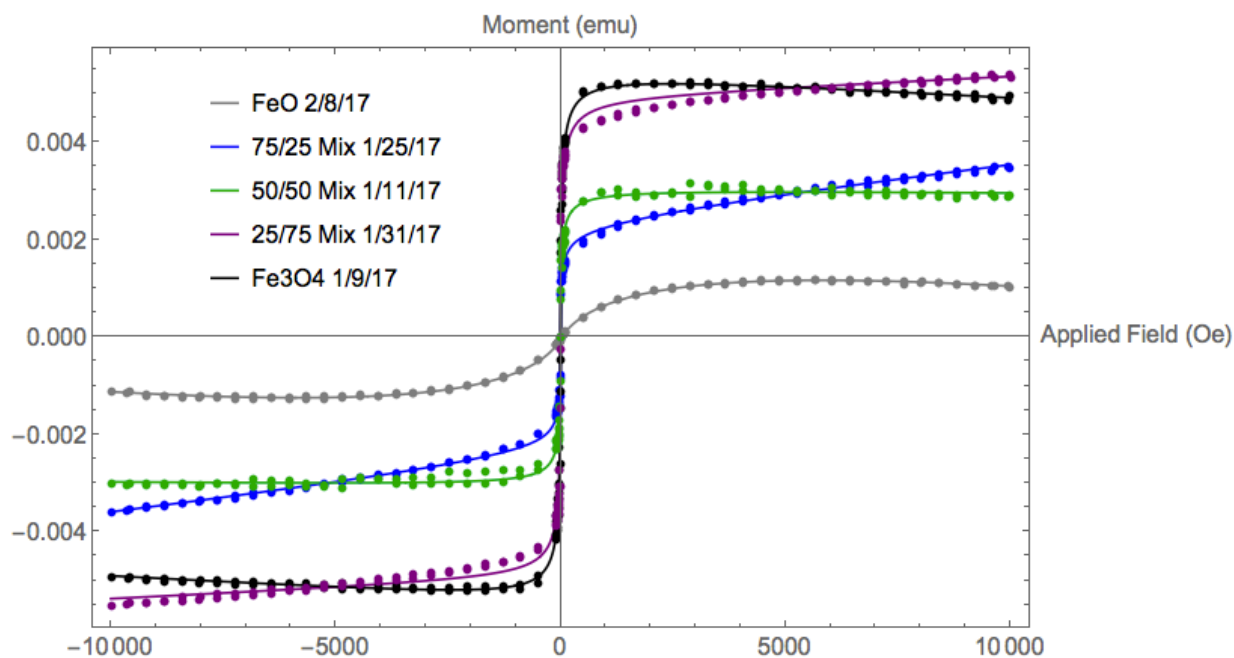


Figure 4.5: The VSM data (dots) and fit curves (lines) for the initial suspensions made of different concentrations of FeO and Fe₃O₄. The legend indicates the composition of each solution by percentages of FeO/Fe₃O₄ in that order, as well as the date each separation was performed.

Mixture of FeO/Fe ₃ O ₄	Percent of VSM signal attributed to FeO	Percent of VSM signal attributed to Fe ₃ O ₄
100% FeO (2/8/17)	100 %	0 %
75% FeO and 25% Fe ₃ O ₄ (1/25/17)	22.9 %	77.1 %
50% FeO and 50% Fe ₃ O ₄ (1/11/17)	1.0 %	99.0 %
25% FeO and 75% Fe ₃ O ₄ (1/31/17)	0 %	100 %
100% Fe ₃ O ₄ (1/9/17)	0 %	100 %

Table 4.2: The percentages of the VSM signal attributed to the two types of particle, based on the DLLMD analysis described in Appendix A. The date the data were taken is given in parentheses.

Unfortunately, some of the data showed changes that were not compatible with this form of analysis, specifically the mixture of 25% FeO and 75% Fe₃O₄. From qualitative observations of the suspensions, we found that all the samples containing Fe₃O₄ had particles that settled to the bottom of the container over the course of a couple of hours. Additionally, upon vigorous shaking of the samples (through sonication) macroscopic clumps of particles were observed, suggesting that the Fe₃O₄ particles were no longer fully dispersed in the fluid. This may have led to groups of particles with a larger magnetic moment than that of the original Fe₃O₄ distribution, resulting in the relatively poor fit in the analysis of certain samples. Notably, the 25% FeO/75% Fe₃O₄ mixture was measured and separated after all the other mixtures containing the first batch of Fe₃O₄ nanoparticles. We hypothesized that the settling behavior may have been a result of incomplete surfactant coating of the particles. This coupled with the high moment value for 22nm particles could have led to too high a dipole-dipole energy, resulting in irreversibly clumped particles. The second batch of Fe₃O₄ particles were synthesized with a smaller average diameter to counteract this problem and were used in all subsequent separation.

The filtrates obtained after separation were measured, and DLLMD analysis indicated that almost all the signal from the filtrate samples resulted from the FeO particles. The fits and VSM data for the filtrate samples of these separations are displayed in Figure 4.6. The lack of signal like that of the Fe₃O₄ particles implies that nearly all the Fe₃O₄ particles aggregated together and fell to the bottom of the channel. However, the settling behavior in suspensions containing Fe₃O₄ particles was observed to take place on time scales smaller

than the duration of each separation. This implies that the behavior of the Fe_3O_4 particles may not have resulted solely due to their larger magnetic moment relative to the FeO particles, but rather due to some difference in their coating that made them less soluble in toluene, as discussed earlier.

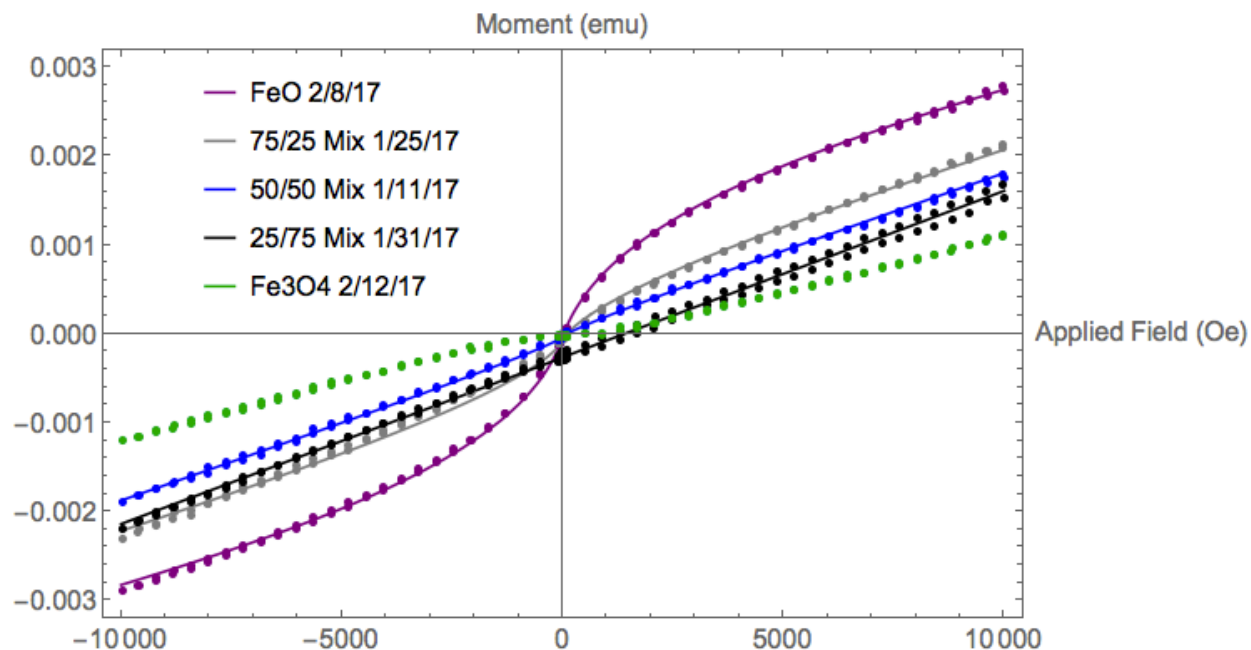


Figure 4.6: The VSM data (dots) and fit curves (lines) for the filtrates of the FeO and Fe_3O_4 mixture separations. The legend indicates the composition of each solution by percentages of FeO/ Fe_3O_4 in that order, as well as the date each separation was performed. We were unable to fit the Fe_3O_4 (green) curve due to high contributions to the signal from the sample holder.

Despite this, we can conclude from the relative uniformity of the filtrates that varying the concentration of the solution does not have a significant impact on the outcome of a separation. We therefore turn to a series of separations based on varying the applied field gradient to further understand the impact of field gradient and pump rate on particle behavior in our setup.

4.3.2 Separations with Varying Field Gradient

For this series of experiments, the smaller (16.76 nm) Fe_3O_4 particles were used due to the irreversible clumping behavior observed in the larger (22.2 nm) Fe_3O_4 particles. In addition, the pump rate was calculated using the high moment particles rather than the median moment particles to minimize the non-magnetic field based settling behavior observed for the first batch of Fe_3O_4 suspensions as just discussed. Initial VSM measurements of the 50% FeO/50% Fe_3O_4 suspensions with varying gradients were taken with the VSM data and fits displayed in Figure 4.7 and the extracted information shown in Table 4.3. As before, the percentages of VSM signal were determined using the method described in Appendix A.

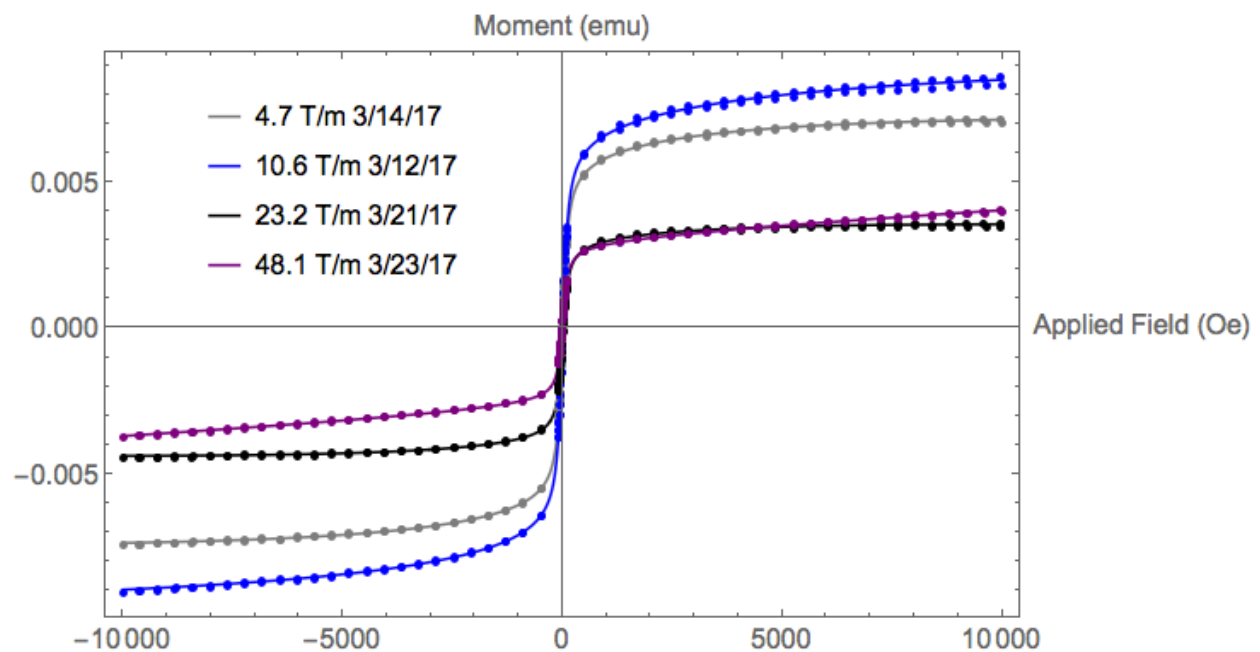


Figure 4.7: The VSM data (dots) and fit curves (lines) for initial suspensions composed of 50% FeO and 50% Fe_3O_4 . The separations were performed on the dates indicated in the legend.

Field Gradient	Percent of VSM signal attributed to FeO	Percent of VSM signal attributed to Fe ₃ O ₄
4.7 T/m (3/14/17)	41.5 %	58.5 %
10.6 T/m (3/12/17)	41.8 %	58.2 %
23.2 T/m (3/21/17)	38.1 %	61.9 %
48.1 T/m (3/23/17)	24.2 %	75.8 %

Table 4.3: The percentages of the VSM signal attributed to the two types of particle, based on the DLLMD analysis described in Appendix A. The date the data were taken is given in parentheses.

Differences in the shape of the curves displayed in Figure 4.7 indicated differences in the samples being measured. This was confirmed in the calculations displayed in Table 4.3 from the signal percentages for the FeO and Fe₃O₄ distributions. The suspensions were created at the same time, but were measured on the dates indicated in the figure and table. A trend can be observed between the date a sample was measured and the amount that its VSM signal matches the curve associated with Fe₃O₄ particles. The XRD measurements indicated that the Fe₃O₄ sample was nearly completely oxidized and no settling/clumping behavior was observed. This implies that the magnetic properties of the FeO nanoparticles were changing over the course of two weeks, most likely due to some slow oxidation process or change in the surface characteristics. This change is likely similar to the changes in VSM signal found in Section 4.2.

In proceeding to then look at performing separations with the array, we accounted for this shift by using the relative change in the FeO signal between each initial sample and its corresponding filtrate, which were prepared and measured on the same day. Qualitative images of each separation are given in Figure 4.8 (A-D) and clearly show that the array is removing an increasing quantity of particles as the field gradient is increased.

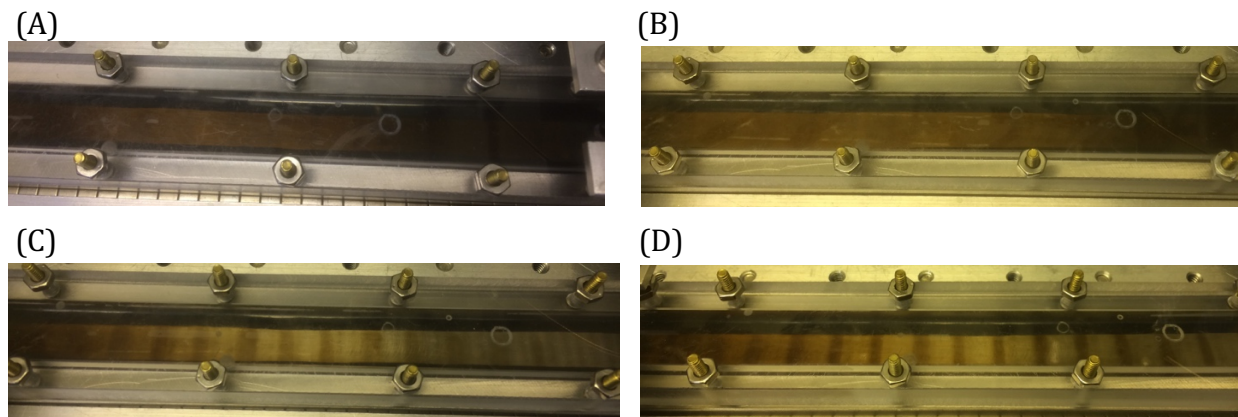


Figure 4.8: Images from separations at field gradients of 4.7 T/m (A), 10.6 T/m (B), 23.2 T/m (C), and 48.1 T/m (D). No banding is observed in (A) or (B), faint and uneven banding is observed in (C), and distinctive even banding is observed in (D).

The filtrates obtained after separation were measured as shown in Figure 4.9, and the results of DLLMD analysis are displayed in Table 4.4. The fits and VSM data for these separations are displayed in Figure 4.9. The VSM signal percentages calculated from the DLLMD scale factors indicate as the applied field gradient increased, so did the percentage of the scale factor associated with the FeO distribution relative to the sum of the scale factors, as shown graphically in Figure 4.10. This indicates that more Fe_3O_4 particles were retained in the channel as the channel was brought closer to the array.

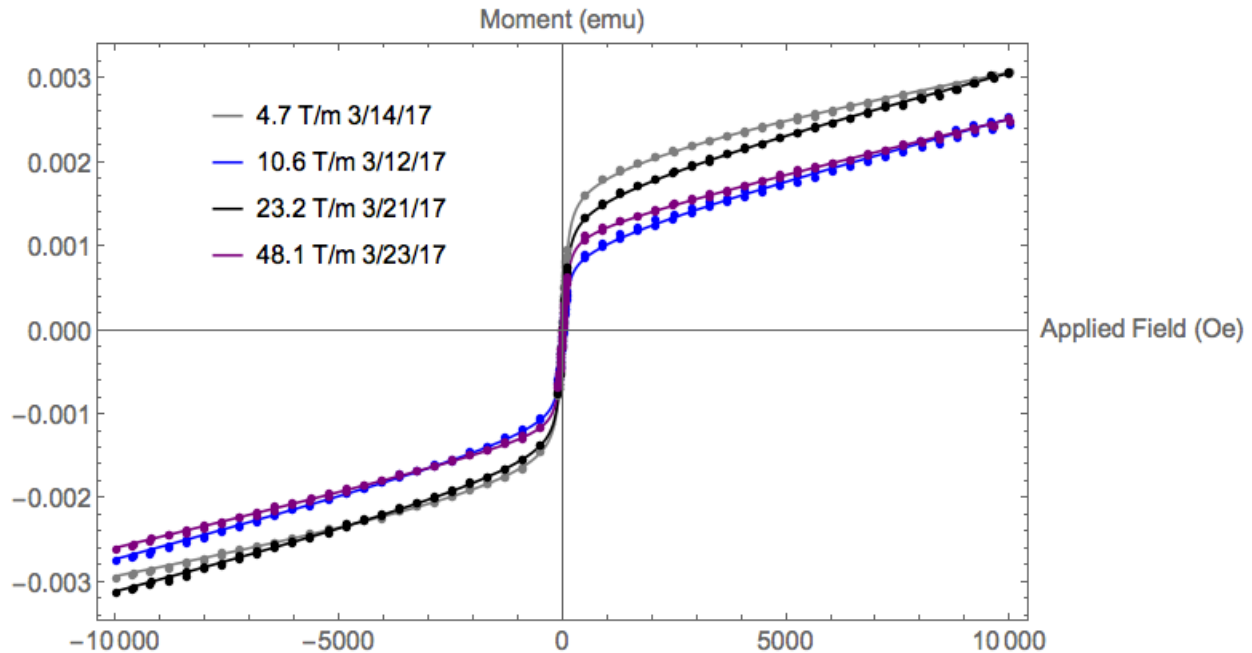


Figure 4.9: The VSM data (dots) and fit curves (lines) for the filtrates of the suspensions composed of 50% FeO and 50% Fe₃O₄, separated under different field gradients. The separations were performed on the dates indicated in the legend.

Field Gradient	Percent of VSM signal attributed to FeO	Percent of VSM signal attributed to Fe ₃ O ₄	Percent change of FeO signal
4.7 T/m (3/14/17)	42.5 %	57.5 %	1.0 %
10.6 T/m (3/12/17)	44.4 %	55.6 %	2.6 %
23.2 T/m (3/21/17)	41.2 %	58.8 %	3.1 %
48.1 T/m (3/23/17)	34.6 %	65.4 %	10.4 %

Table 4.4: The percentages of the VSM signal attributed to the two types of particle, based on the DLLMD analysis described in Appendix A, as well as the percentage change of the distributions relative to the initial samples. The date the data were taken is given in parentheses.

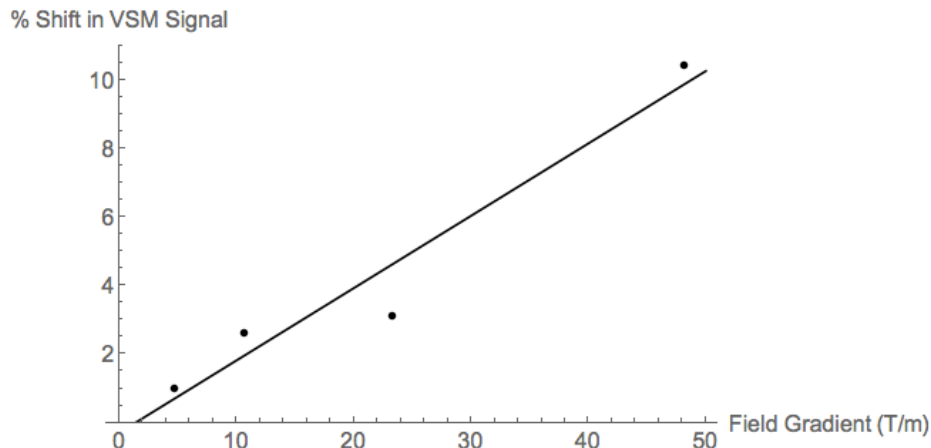


Figure 4.10: A plot of the percentage shift of signal from Fe_3O_4 to FeO vs. applied field gradient. A linear fit is indicated by the black line.

4.4 Receiver Operating Characteristic Analysis

As suggested in Chapter 2, we expected to perform ROC analysis on the results of our separations by measuring the number of FeO and Fe_3O_4 particles before the separation and in the filtrate after the separation. As indicated by Table 2.1, we could obtain the TPF (true positive fraction) using Equation 2.15 by considering these numbers for the FeO particles, and similarly we could obtain the FPF (false positive fraction) using Equations 2.16 and 2.17 by considering these numbers for the Fe_3O_4 particles. Unfortunately, we are unable to perform this analysis at this time, as the VSM data obtained for the two series of separations alone have proved insufficient as detailed more completely below.

For the separations of solutions with varying particle concentrations, the similarities in VSM signal from the filtrates did not provide enough information to determine relative changes in the FeO particle concentration. More critically, all the VSM data from the filtrates of this series indicated that essentially no Fe_3O_4 particles remained in solution, which would mean that the FPF would equal zero. This prevents the construction of an ROC curve, as all the associated data points for this series would be located along the y-axis for graphs of TPF versus FPF. While such a curve would reflect the significant clumping and sample degradation, it would not indicate the device performance.

For the separations of solutions with varying applied field gradient, the reduction in Fe₃O₄-like signal does provide enough information to calculate the FPF by comparing the initial and final samples. The FPF values are given in Table 4.5 and would provide enough information to form a curve given the TPF values. However, the VSM data alone provide no insight into the number of FeO particles that aggregated during solution as it is difficult to retrieve the residue portion without a change in concentration due to the need for additional solvent. Additionally, acquiring aggregated particles proved difficult, as once the particles had come out of solution we had no direct way of re-agitating them back into suspension such as through sonication. This therefore prevented the calculation of the TPF without further correlating information.

Field Gradient	FPF (filtrate Fe ₃ O ₄ %/initial Fe ₃ O ₄ %)
4.7 T/m (3/14/17)	0.98
10.6 T/m (3/12/17)	0.96
23.2 T/m (3/21/17)	0.95
48.1 T/m (3/23/17)	0.86

Table 4.5: The false positive fraction (the percent of Fe₃O₄ particles that end up in the filtrate) for the series of separations performed at varying field gradients.

However, provided additional data about the number of particles in the initial solutions and the filtrates through XRD and AAS measurement, an ROC curve could be constructed in this case, given the experimental results we have demonstrated up to now. We were able to calculate the TPF and FPF for one of the separations from such measurements provided by our collaborators at CWRU, as indicated by the blue point in Figure 4.11, but encountered problems with the other due to changes in the particle concentration. Completing such an endeavor would be valuable in quantifying the efficiency of the Halbach array as a sorting mechanism, and we are working on a new set of separations to pursue that goal.

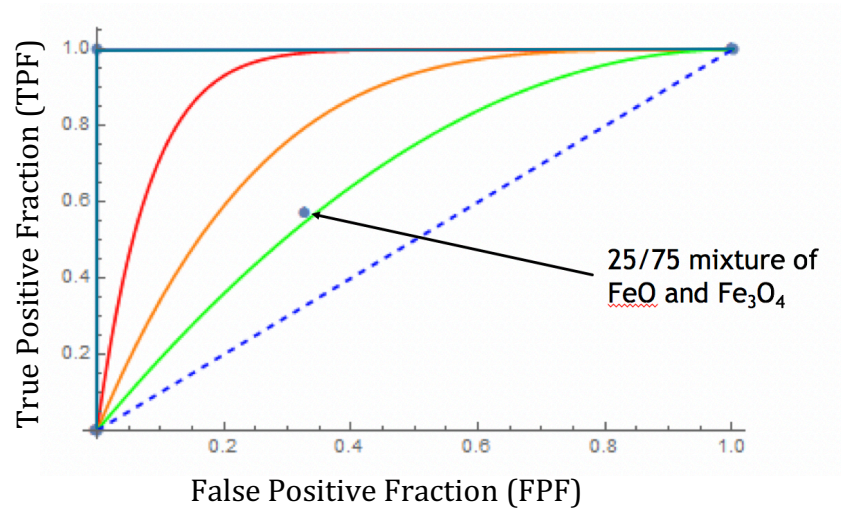


Figure 4.11: Figure 2.5 of example ROC curves with the addition of the TPF and FPF point calculated from the XRD and AAS measurements of the 25% FeO/75% Fe₃O₄ mixture.

Chapter 5

Conclusions and Future Work

5.1 Conclusions

Particle uniformity is essential for the application of magnetic nanoparticles to a variety of developing biomedical technologies and procedures. This thesis has worked to characterize the ability of a linear inverted Halbach array to separate out nanoparticles of differing magnetic moments under two regimes, one of varying particle concentration separated at a single field gradient, and one of a single particle concentration separated at varying field gradients. We have developed quantitative methods for analyzing the data obtained before and after each separation based on an assumed lognormal distribution of magnetic moments. We have also shown how these methods may be used to apply ROC analysis to quantify the use of the Halbach array as a sorting mechanism.

Our results from varying particle concentration indicated that as expected, particle behavior in the presence of the Halbach array is affected primarily by the field gradient and pump rate experienced by the particles, and not the number of particles present in the channel. However, our results are hindered by the changes of magnetic signal observed in

the FeO suspension and the settling behavior observed in the Fe₃O₄ suspension; these sample issues cloud further interpretation of the data.

Our results from varying field gradient indicated a positive linear relationship between the percent of Fe₃O₄ particles that aggregated out of the filtrate and an increase in the field gradient, which was additionally confirmed qualitatively. These results begin the process of a more complete characterization of the array as a sorting mechanism. Unfortunately, the information extracted through our analysis methods was insufficient for constructing an ROC curve, and further structural characterization of the resulting solutions is necessary.

5.2 Future Work

The samples used in this thesis underwent structural characterization through the assistance of our collaborators at CWRU, but changes in the particle concentration of our samples prevented us from making full use of this analysis. Subsequent experimentation, structural characterization, and use of ROC analysis will provide further insights into the efficiency of the inverted linear Halbach array as a nanoparticle sorting mechanism.

From the results of our experimental efforts, we conclude that there are three factors impeding the clarity of our characterization of the array: the change in the nanoparticles over time, the physical interpretation of our DLLMD analysis, and the nature of the channel design.

As evidenced in Chapter 4, changes in the nanoparticle samples, which were held in anhydrous toluene in an argon glovebox until use, occurred over the span of a couple of weeks. This implies that the uniformity of the magnetic properties of a suspension of nanoparticles may apply for a limited time, decreasing the utility of any single batch of nanoparticles. While this may not pose a problem for one-time use biomedical processes, it is an impediment to industrial synthesis, purification, and characterization of nanoparticles. Particles that are so processed may not arrive at their destination in the same state, which could be problematic for applications sensitive to changes in the particles magnetic

properties, such as therapeutic hyperthermia. Therefore, we may need to evaluate the array with particles prepared in a different fashion.

Currently, our method for analyzing a sample containing two types of particles requires measurements and analysis of each type individually. This strategy does not allow for changes of the particles over time, and employs the so called “scale factors”. In the single moment Langevin model, the normalization constants consist of the number of particles multiplied by the single magnetic moment. However, the scale factor cannot be equivalent to these normalization constants, as in our model the particle magnetic moment is no longer considered a constant. Further analysis of the impact of the scale factor on the model may lead to a physical conclusion, and may help clarify the difficulties encountered when attempting to calculate the TPF for the series of separations performed with varying field gradients.

As mentioned in Section 4.4, aggregated particles remain difficult to acquire from the channel wall without changes in concentration. We therefore suggest that improvements might be made to increase particle recovery following the separation processes. One possibility would be to replace the current base plate with a different material, ideally one that would facilitate particle recovery. Another possibility would be to redesign the channel in such a way that it could be placed in a sonicating bath, energizing the particles and re-suspending them in the carrier fluid.

Bibliography

1. (Beveridge et al.)

J. S. Beveridge, J. R. Stephens, and M. E. Williams, "Differential magnetic catch and release: experimental parameters for controlled separation of magnetic nanoparticles," *Analyst*, vol. 136, no. 12, pp. 2564–2571, 2011.

2. (Booth)

R. a. Booth, "Inter- and Intraparticle Interactions in Magnetic Nanoparticle Systems," Ph.D. Thesis, Dept. Phys., Carnegie Melon Univ., Pittsburgh, PA, 2012

3. (Carpino et al.)

F. Carpino, L. R. Moore, M. Zborowski, J. J. Chalmers, and P. S. Williams, "Analysis of magnetic nanoparticles using quadrupole magnetic field-flow fractionation," *J. Magn. Magn. Mater.*, vol. 293, no. 1, pp. 546–552, May 2005.

4. (Chantrell)

R. w. Chantrell, J. Popplewell, and S. w. Charles, "Measurements of particle size distribution parameters in ferrofluids," in *IEEE Transactions on Magnetics*, 1978, vol. MAG-14, pp. 975–977.

5. (Chen et al.)

D.-X. Chen, A. Sanchez, E. Taboada, A. Roig, N. Sun, and H.-C. Gu, "Size determination of superparamagnetic nanoparticles from magnetization curve," *J. Appl. Phys.*, vol. 105, no. 8, p. 83924, Apr. 2009.

6. (Cuevas et al.)

G. De Las Cuevas, J. Faraudo, and J. Camacho, "Low-gradient magnetophoresis through field-induced reversible aggregation," *J. Phys. Chem. C*, vol. 112, no. 4, pp. 945–950, Jan. 2008.

7. (Cullity)

B. D. Cullity and C. D. Graham, *Introduction to Magnetic Materials*, 2 edition. Hoboken, N.J: Wiley-IEEE Press, 2008.

8. (Faraudo et al.)

J. Faraudo, J. S. Andreu, and J. Camacho, "Understanding diluted dispersions of superparamagnetic particles under strong magnetic fields: a review of concepts, theory and simulations," *Soft Matter*, vol. 9, no. 29, pp. 6654–6664, 2013.

9. (Ferguson et al.)

R. m. Ferguson, K. r. Minard, A. p. Khandhar, and K. m. Krishnan, "Optimizing magnetite nanoparticles for mass sensitivity in magnetic particle imaging," *Medical Physics*, vol. 38, no. 3, pp. 1619–1626, Mar. 2011.

10. (Franklin)

T. a. Franklin, "Ferofluid Flow Phenomena," M.S. Thesis, Dept. of Elec. Eng. and Comp. Science, MIT, Cambridge, MA, 2003

11. (Gehrcke)

JP Gehrcke, "Characterization of the Magnetic Particle Imaging Signal Based on Theory, Simulation, and Experiment," M.S. Thesis, Exp. Phys., Univ. of Würzburg, Germany, 2010.

12. (Gersten and Smith)

J. Gersten and F. Smith, *The Physics and Chemistry of Materials by Gersten Joel I Smith Frederick W - AbeBooks*. John Wiley & Sons, inc., 2001.

13. (Haefeli and Chastellian)

V. P. Torchilin, U. O. Haefeli, and M. Chastellian, *Nanoparticulates as Drug Carriers*. Imperial College Press, 2006.

14. (Halbach)

K. Halbach, "Design of Permanent Multipole Magnets with Oriented Rare-Earth Cobalt Material," *Nuclear Instruments & Methods*, vol. 169, no. 1, pp. 1–10, 1980.

15. (Hayden and Haefeli)

M. E. Hayden and U. O. Haefeli, "'Magnetic bandages' for targeted delivery of therapeutic agents," *J. Phys.-Condes. Matter*, vol. 18, no. 38, pp. S2877–S2891, Sep. 2006.

16. (Hoyos et al.)

M. Hoyos, L. Moore, P. S. Williams, and M. Zborowski, "The use of a linear Halbach array combined with a step-SPLITT channel for continuous sorting of magnetic species," *J. Magn. Mater.*, vol. 323, no. 10, pp. 1384–1388, May 2011.

17. (Ijiri et al.)

Y. Ijiri, C. Poudel, P. S. Williams, L. R. Moore, T. Orita, and M. Zborowski, "Inverted Linear Halbach Array for Separation of Magnetic Nanoparticles," *IEEE Trans. Magn.*, vol. 49, no. 7, pp. 3449–3452, Jul. 2013.

18. (Ito et al.)

A. Ito, M. Shinkai, H. Honda, and T. Kobayashi, "Medical application of functionalized magnetic nanoparticles," *J. Biosci. Bioeng.*, vol. 100, no. 1, pp. 1–11, Jul. 2005.

19. (Kakay et al.)

A. Kakay, M. W. Gutowski, L. Takacs, V. Franco, and L. K. Varga, "Langevin granulometry of the particle size distribution," *J. Phys. A-Math. Gen.*, vol. 37, no. 23, pp. 6027–6041, Jun. 2004.

20. (Krishnan)

K. M. Krishnan, "Biomedical Nanomagnetism: A Spin Through Possibilities in Imaging, Diagnostics, and Therapy," *IEEE Trans. Magn.*, vol. 46, no. 7, pp. 2523–2558, Jul. 2010.

21. (Malekzadeh et al.)

A. M. Malekzadeh, A. Ramazani, S. J. T. Rezaei, and H. Niknejad, "Design and construction of multifunctional hyperbranched polymers coated magnetite nanoparticles for both targeting magnetic resonance imaging and cancer therapy," *J. Colloid Interface Sci.*, vol. 490, pp. 64–73, Mar. 2017.

22. (Meeker)

D. Meeker. *Finite element method magnetics*. Version 4.2 (1 April 2009 Build). 2010

23. (Orita et al.)

T. Orita, L. R. Moore, P. Joshi, M. Tomita, T. Horiuchi, and M. Zborowski, "A Quantitative Determination of Magnetic Nanoparticle Separation Using On-Off Field Operation of Quadrupole Magnetic Field-Flow Fractionation (QMgFFF)," *Anal. Sci.*, vol. 29, no. 7, pp. 761–764, Jul. 2013.

24. (Pankhurst et al.)

Q. a. Pankhurst, N. k. t. Thanh, S. k. Jones, and J. Dobson, "Progress in applications of magnetic nanoparticles in biomedicine," *Journal of Physics D: Applied Physics*, vol. 42, no. 22, p. 224001, Nov. 2009.

25. (Poudel)

C. Poudel, "Linear Inverted Halbach Array for the Separation of Magnetic Nanoparticles," Undergrad Thesis, Dept. of Phys. and Astro., Oberlin College, Oberlin, OH, 2014

26. (Samia 2013)

M. H. Pablico-Lansigan, S. F. Situ, and A. C. S. Samia, "Magnetic particle imaging: advancements and perspectives for real-time in vivo monitoring and image-guided therapy," *Nanoscale*, vol. 5, no. 10, pp. 4040–4055, 2013.

27. (Samia 2016)

S. F. Situ, J. Cao, C. Chen, E. C. Abenojar, J. M. Maia, and A. C. S. Samia, "Reactive Extrusion Strategies to Fabricate Magnetite-Polyethylene Nanocomposites with Enhanced Mechanical and Magnetic Hyperthermia Properties," *Macromol. Mater. Eng.*, vol. 301, no. 12, pp. 1525–1536, Dec. 2016.

28. (Singamaneni et al.)

S. Singamaneni, V. N. Bliznyuk, C. Binek, and E. Y. Tsymbal, "Magnetic nanoparticles: recent advances in synthesis, self-assembly and applications," *Journal of Materials Chemistry*, vol. 21, no. 42, p. 16819, 2011.

29. (Stephens et al.)

J. r. Stephens, J. s. Beveridge, and M. e. Williams, "Analytical methods for separating and isolating magnetic nanoparticles," *Physical Chemistry Chemical Physics*, vol. 14, no. 10, pp. 3280–3289, Jan. 2012.

30. (Tasci et al.)

T. O. Tasci, E. Manangon, D. P. Fernandez, W. P. Johnson, and B. K. Gale, "Separation of Magnetic Nanoparticles by Cyclical Electrical Field Flow Fractionation," *IEEE Trans. Magn.*, vol. 49, no. 1, pp. 331–335, Jan. 2013.

31. (Van Reenan)

A. van Reenen *et al.*, "Accurate quantification of magnetic particle properties by intra-pair magnetophoresis for nanobiotechnology," *Appl. Phys. Lett.*, vol. 103, no. 4, p. 43704, Jul. 2013.

32. (Williams et al. 1)

P. S. Williams, F. Carpino, and M. Zborowski, "Magnetic Nanoparticle Drug Carriers and Their Study by Quadrupole Magnetic Field-Flow Fractionation," *Mol. Pharm.*, vol. 6, no. 5, pp. 1290–1306, Oct. 2009.

33. (Williams et al. 2)

P. S. Williams, F. Carpino, and M. Zborowski, "Characterization of magnetic nanoparticles using programmed quadrupole magnetic field-flow fractionation," *Philos. Trans. R. Soc. A-Math. Phys. Eng. Sci.*, vol. 368, no. 1927, pp. 4419–4437, Sep. 2010.

34. (Yavuz et al.)

C. T. Yavuz *et al.*, "Low-field magnetic separation of monodisperse Fe₃O₄ nanocrystals," *Science*, vol. 314, no. 5801, pp. 964–967, Nov. 2006.

Appendix A

Mathematica Code for VSM Analysis

The following is the template of code used to analyze the magnetometry data using a modified Langevin equation model described in Chapter 2. It was written in Mathematica, a computational software program, and the inputs were changed to match each set of VSM data. Presented below are both the single Langevin and the double Langevin lognormal moment distribution model (SLLMD and DLLMD respectively), as well as a single Langevin, single moment model (SLSM) for comparison. The assumption of a lognormal distribution in moment for each sample was based on previous data related to the synthesis of magnetic nanoparticles (Kakay et al.), and is incorporated into the Langevin equation in the SLLMD and DLLMD models. The DLLMD model was used to analyze solutions containing a mixture of two different types of particles. A SLLMD analysis was performed on each of the solutions used in the mixture, and the results of that analysis were used in the DLLMD model.

Each analysis took the same basic form, beginning with a plot of both the data set and the potential fit function. This method was used to obtain starting values for each variable, which were then plugged into the FindFit function, which used χ^2 analysis to find the values that best fit the data. The accuracy of the fit was then confirmed by plotting the new fit function with the data set, and any relevant data were extracted from the fit values. For the SLLMD model, the fit variables were s , μ , σ , the slope, and the offset, where s represents the scale factor, and μ is the mean and σ is the standard deviation of the normal distribution on which the lognormal distribution is based. The slope represents the magnetic contribution of the sample holder or carrier fluid and the offset accounts for any errors in centering the sample between the detection coils of the VSM. The median magnetic moment of the sample was determined by taking the median of the lognormal distribution defined by μ and σ . The magnetic moment of desired portions of the distribution, namely the 20th and 90th percentile, were obtained in a similar manner.

For the DLLMD model, the fit variables were s_1 , s_2 , the slope, and the offset, where s_1 and s_2 represent the scale factor for distribution 1 and distribution 2 respectively. This model requires SLLMD analysis on the two types of particles used, with μ_1 and σ_1 corresponding to the fit values for the first distribution, and μ_2 and σ_2 corresponding to the fit values for the second distribution. The percentage of VSM signal from each type of particle was obtained by finding the percentage of each scale factor in comparison to the sum of the scale factors.

Data Import

```
(*These are instructions for fitting magnetometry data.*)
Import[
  "C:\\Users\\moment\\Documents\\Your stuff\\Your folder (optional)\\Your file.xlsx"]
(*Specify the data file and import it. The data works better if you
import it from an Excel file, which is why "Your file" ends in .xlsx.*)

(*data*) = (*Insert the data set just imported here. Make sure there isn't an
extra set of curly brackets around it because Mathematica will not accept.*);

k = 4.1 * 10^-14; (*This is your value of kBT, the thermal energy,
which we say is constant for this experiment. Before running any of the fits,
make sure to store this value.*)
```

Single Moment Model

```
Langevin[h_] := n * m * (Coth[m * h / k] - k / (m * h))
(*This is the Langevin equation as defined in Chapter 2,
where n means the number of particles, m is the magnetic particle moment, and the
slope adjusts for any paramagnetic or diamagnetic signal from the sample holder.*)

Show[Plot[Langevin[h] + (*slope*) * h, {h, -10000, 10000}], ListPlot[(*data*)]]
(*Change your guesses of n, m, and the slope,
along with whatever the name of the dataset is for data. This will
help you eyeball the fit so you have starting guess values later.*)

FindFit[(*data*), n * m * (Coth[m * h / k] - k / (m * h)) + l * h,
  {{n, (*startval*)}, {m, (*startval*)}, {l, (*startval*)}}, h]
(*Plug in your starting guess values for n, m, and l wherever it says startval,
and the name of your dataset where it says data. It's going to give you some error
messages and take some time (5-15 minutes, more if you have bad startvals),
but eventually it will pop out the best fit values for the three parameters.*)

Show[Plot[(*n*) * (*m*) * [Coth[(*m*) * h / k] - k / ((*m*) * h)] + (*slope*) * h,
  {h, -10000, 10000}], ListPlot[(*data*)]]
(*Same thing you did before for eyeballing the fit,
only now you plug in the values that you just got for the
parameters. This is just so you can see how well the fit was approximated.*)
```

Log-normal Moment Distribution Model

```
pdfLangevin(*I*) [h_?NumericQ] :=
  NIntegrate[PDF[LogNormalDistribution[(*μ*), (*σ*)], m] *
    (Coth[m * h / k] - k / (m * h)), {m, 0, 10^-12}]
(*Adjust the name of this function if you are working with more than one set
of data in one notebook by changing the I to the appropriate identifying letter*)
```

```
Show[Plot[(*s*) * pdfLangevin[h] + (*slope*) * h, {h, -10000, 10000}],
ListPlot[(*data*)]]
(*Change your guesses of s,  $\mu$ , and  $\sigma$ , along with whatever the name of
the dataset is for data. This will help you eyeball the fit so you have
starting guess values later. Here, s means saturation value or scale factor,
 $\mu$  is the mean of the normal distribution that the lognormal fit is derived from,
and  $\sigma$  is the standard deviation of this normal distribution,
and controls the variance.*)

FindFit[(*data*), s * NIntegrate[
  PDF[LogNormalDistribution[ $\mu$ ,  $\sigma$ ], m] * (Coth[m * h / k] - k / (m * h)), {m, 0, 10-12}] + l * h,
  {{s, (*startval*)}, { $\mu$ , (*startval*)}, { $\sigma$ , (*startval*)}, {l, (*startval*)}}, h]
(*Plug in your starting guess values for s,  $\mu$ , and  $\sigma$  wherever it says startval,
and the name of your dataset where it says data. It's going to give you some error
messages and take some time (5-15 minutes, more if you have bad startvals),
but eventually it will pop out the best fit values for the three parameters.*)

Show[Plot[(*s*) * NIntegrate[PDF[LogNormalDistribution[(* $\mu$ *), (* $\sigma$ *)], m] *
  (Coth[m * h / k] - k / (m * h)), {m, 0, 10-12}] +
  (*slope*) * h, {h, -10000, 10000}], ListPlot[(*data*)]]
(*Same thing you did before for eyeballing the fit,
only now you plug in the values that you just got for the
parameters. This is just so you can see how well the fit was approximated.*)

Median[LogNormalDistribution[(* $\mu$ *), (* $\sigma$ *)]]

Probability[x < (*moment*), x  $\approx$  LogNormalDistribution[(* $\mu$ *), (* $\sigma$ *)]]
(*For checking the median of your distribution and what
percentile various moment values are. Useful once you start calculating
separation parameters in the Excel file. Values should be in emu.*)
```

Log-normal Moment Distribution Double Langevin Model

```
pdfLangevin(*I1*) [h_?NumericQ] :=
  NIntegrate[PDF[LogNormalDistribution[(* $\mu$ 1*), (* $\sigma$ 1*)], m] *
    (Coth[m * h / k] - k / (m * h)), {m, 0, 10-12}]
(*Adjust the name of this function by changing the I1 and
I2 to the appropriate identifying letter,
and plug in the  $\mu$  and  $\sigma$  values that match the two distributions you are combining,
distribution 1 and distribution 2 respectively.*)

pdfLangevin(*I2*) [h_?NumericQ] :=
  NIntegrate[PDF[LogNormalDistribution[(* $\mu$ 2*), (* $\sigma$ 2*)], m] *
    (Coth[m * h / k] - k / (m * h)), {m, 0, 10-12}]
```

```
Show[Plot[(*s1*) * pdfLangevin(*I1*) [h] + (*s2*) * pdfLangevin(*I2*) [h] +
  (*slope*) * h + (*offset*), {h, -10000, 10000}], ListPlot[(*data*)]]
(*Change your guesses of s1, s2, the slope and offset,
along with whatever the name of the dataset is for data. This will
help you eyeball the fit so you have starting guess values later. Here,
s means saturation value or scale factor,
μ is the mean of the normal distribution that the lognormal fit is derived from,
and σ is the standard deviation of this normal distribution, and controls the variance.*)
```

```
FindFit[(*data*), s1 * NIntegrate[
  PDF[LogNormalDistribution[μ1, σ1], m] * (Coth[m * h / k] - k / (m * h)), {m, 0, 10-12}] +
  s2 * NIntegrate[PDF[LogNormalDistribution[μ2, σ2], m] * (Coth[m * h / k] - k / (m * h)),
  {m, 0, 10-12}] + 1 * h + g, {{s1, (*startval*)},
  {s2, (*startval*)}, {1, (*startval*)}, {g, (*startval*)}}, h]
(*Plug in your starting guess values for s1, s2, the slope,
and the offset wherever it says startval, and the name of your dataset where it
says data. It's going to give you some error messages and take a minute or two,
and eventually it will pop out the best fit values for the three parameters.*)
```

```
Show[Plot[(*s1*) * NIntegrate[PDF[LogNormalDistribution[(*μ1*), (*σ1*)], m] *
  (Coth[m * h / k] - k / (m * h)), {m, 0, 10-12}] +
  (*s2*) * NIntegrate[PDF[LogNormalDistribution[(*μ2*), (*σ2*)], m] *
  (Coth[m * h / k] - k / (m * h)), {m, 0, 10-12}] + (*slope*) * h +
  (*offset*), {h, -10000, 10000}], ListPlot[(*data*)],
  AxesLabel → {"Field (Oe)", "Moment (emu)"}]
(*Same thing you did before for eyeballing the fit,
only now you plug in the values that you just got for the
parameters. This is just so you can see how well the fit was approximated.*)
```

Percent of VSM signal from Langevin 1

$$\frac{s_1}{s_1 + s_2}$$

(*This should give you approximately the amount
of signal the VSM receives from the 1st distribution*)

Percent of VSM signal from Langevin 2

$$\frac{s_2}{s_1 + s_2}$$

(*This should give you approximately the amount
of signal the VSM receives from the 2nd distribution*)

$$\frac{s_1}{s_2}$$

(*This gives a ratio of the two distributions*)

Example and Comparison

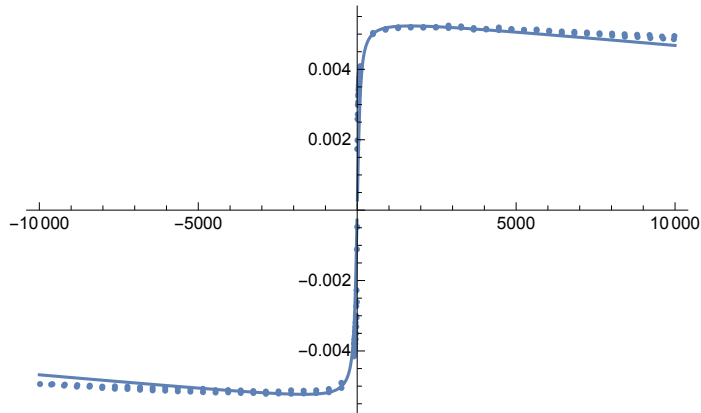
Below is a comparison of the two methods, the first modeling an example set of data by assuming a single magnetic moment, and the second modeling the same data set by assuming a lognormal distribu-

tion of magnetic moments.

Single Moment Langevin

```
Langevin[h_] := 5.5 * 1012 * 10-15 * (Coth[10-15 * h / k] - k / (10-15 * h))
```

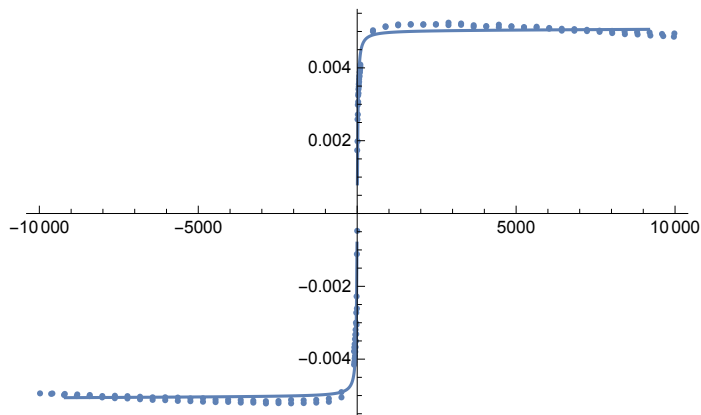
```
Show[Plot[Langevin[h] - 8 * 10-8 * h, {h, -10000, 10000}], ListPlot[Fe304orig]]
```



```
FindFit[Fe304orig, n * m * (Coth[m * h / k] - k / (m * h)) + 1 * h,
  {{n, 5.5 * 1012}, {m, 10-15}, {1, -8 * 10-8}}, h]
```

```
{n → 1.58678 * 1012, m → 3.17244 * 10-15, 1 → 3.46227 * 10-9}
```

```
Show[Plot[1.5867814037991392` * 1012 * 3.17244122984884` * 10-15 *
  (Coth[3.17244122984884` * 10-15 * h / k] - k / (3.17244122984884` * 10-15 * h)) +
  3.462266511992397` * 10-9 * h, {h, -10000, 10000}], ListPlot[Fe304orig]]
```



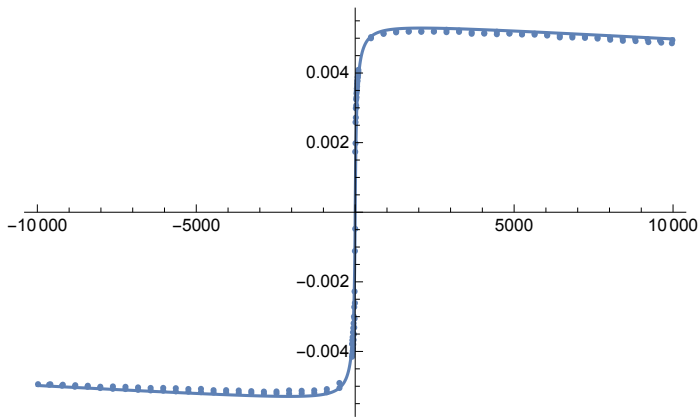
Lognormal Moment Distribution Langevin

```
pdfLangevinfe304[h_?NumericQ] :=
```

```
NIntegrate[
```

```
PDF[LogNormalDistribution[-34, 1], m] * (Coth[m * h / k] - k / (m * h)), {m, 0, 10-12}]
```

```
Show[Plot[0.0055 * pdfLangevinfe304[h] - 5 * 10^-8 * h, {h, -10000, 10000}],
ListPlot[Fe304orig]]
```



```
FindFit[Fe304orig,
s * NIntegrate[PDF[LogNormalDistribution[μ, σ], m] * (Coth[m * h / k] - k / (m * h)),
{m, 0, 10^-12}] + l * h, {{s, 0.0055}, {μ, -34}, {σ, 1}, {l, -5 * 10^-8}}, h]
```

NIntegrate: The integrand $\left(-\frac{4.1 \times 10^{-14}}{h m} + \text{Coth}[2.43902 \times 10^{13} h m]\right) \left(\left\{\begin{array}{l} \frac{e^{-\frac{1}{2} \text{Power}[\ll 2 \gg] \text{Power}[\ll 2 \gg]}}{m \sqrt{2 \pi} \sigma} \quad m > 0 \\ 0 \quad \text{True} \end{array}\right.\right)$ has evaluated to

non-numerical values for all sampling points in the region with boundaries $\left\{\left\{0, \frac{1}{1000000000000000}\right\}\right\}$.

NIntegrate: The integrand $\left(-\frac{4.11514 \times 10^{-18}}{m} + \text{Coth}[2.43005 \times 10^{17} m]\right) \left(\left\{\begin{array}{l} \frac{e^{-\frac{1}{2} \text{Power}[\ll 2 \gg] \text{Power}[\ll 2 \gg]}}{m \sqrt{2 \pi} \sigma} \quad m > 0 \\ 0 \quad \text{True} \end{array}\right.\right)$ has evaluated to

non-numerical values for all sampling points in the region with boundaries $\left\{\left\{0, \frac{1}{1000000000000000}\right\}\right\}$.

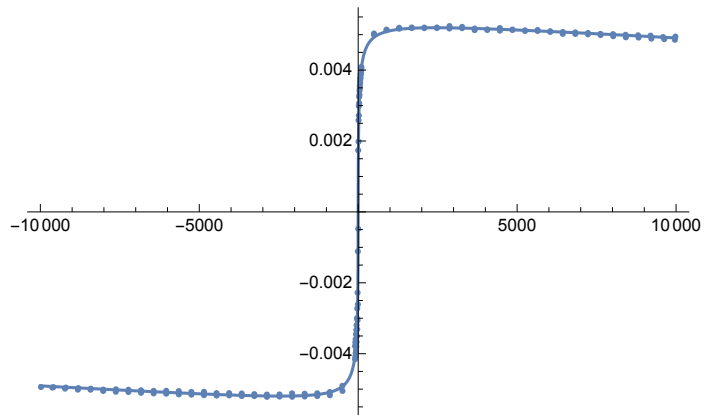
NIntegrate: The integrand $\left(-\frac{4.25832 \times 10^{-18}}{m} + \text{Coth}[2.34834 \times 10^{17} m]\right) \left(\left\{\begin{array}{l} \frac{e^{-\frac{1}{2} \text{Power}[\ll 2 \gg] \text{Power}[\ll 2 \gg]}}{m \sqrt{2 \pi} \sigma} \quad m > 0 \\ 0 \quad \text{True} \end{array}\right.\right)$ has evaluated to

non-numerical values for all sampling points in the region with boundaries $\left\{\left\{0, \frac{1}{1000000000000000}\right\}\right\}$.

General: Further output of NIntegrate::inumr will be suppressed during this calculation.

```
{s → 0.00547502, μ → -33.3226, σ → 1.91298, l → -5.19952 * 10^-8}
```

```
Show[
  Plot[0.0054750237751093065` * NIntegrate[PDF[LogNormalDistribution[-33.32256712064471`,
    1.9129827701272757`], m] * (Coth[m * h/k] - k / (m * h)), {m, 0, 10^-12}] -
    5.199524268171383` * ^-8 * h, {h, -10 000, 10 000}], ListPlot[Fe304orig]]
```



```
Median[LogNormalDistribution[-33.32256712064471`, 1.9129827701272757`]]
```

3.37437×10^{-15}

```
Probability[x < 4 * 10^-14,
  x ≈ LogNormalDistribution[-33.32256712064471`, 1.9129827701272757`]]
```

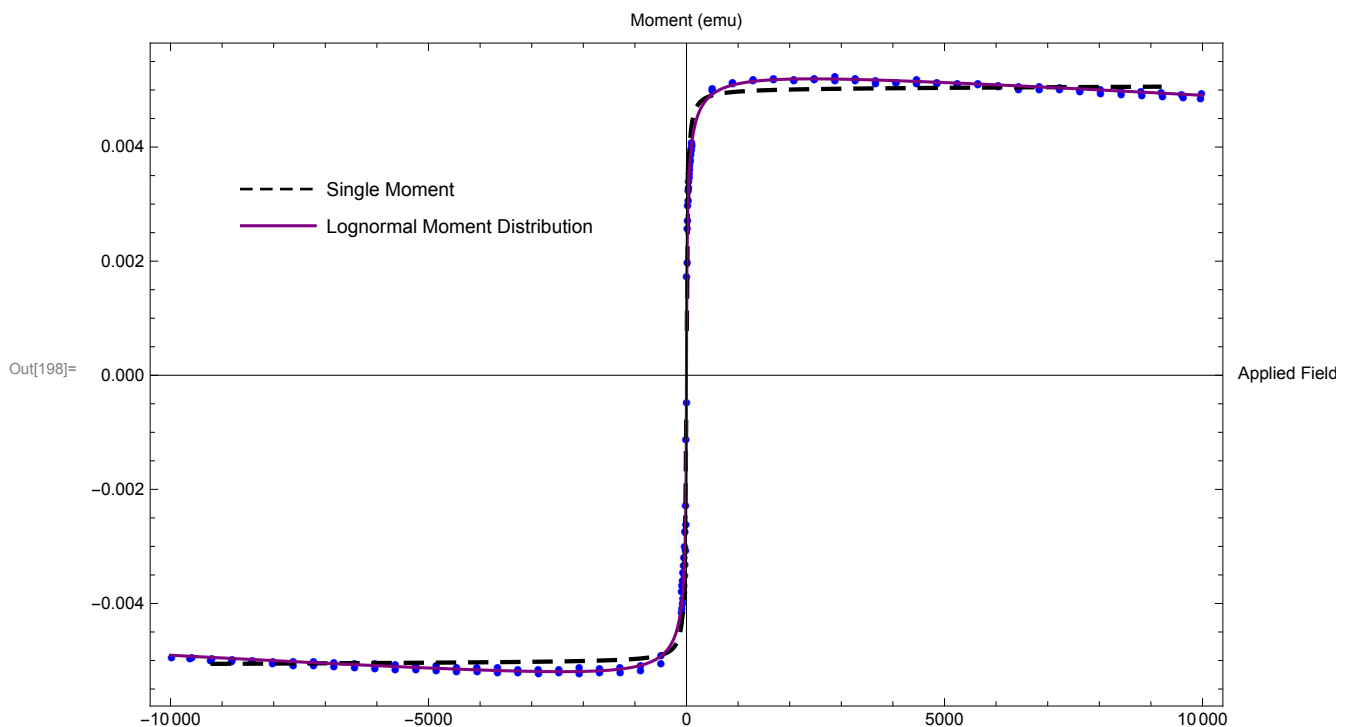
0.901921

Comparison

```

In[198]:= Show[ListPlot[Fe304orig, PlotStyle -> {Blue}, PlotMarkers -> {Automatic, Tiny}],
  Plot[{1.5867814037991392` * ^12 * 3.17244122984884` * ^-15 *
    (Coth[3.17244122984884` * ^-15 * h / k] - k / (3.17244122984884` * ^-15 * h)) +
    3.462266511992397` * ^-9 * h, 0.0054750237751093065` *
    NIntegrate[PDF[LogNormalDistribution[-33.32256712064471`, 1.9129827701272757`], m] *
    (Coth[m * h / k] - k / (m * h)), {m, 0, 10^-12}] - 5.199524268171383` * ^-8 * h},
  {h, -10000, 10000}, PlotStyle -> {{Black, Thickness[0.004], Dashing[0.015]}, {Purple}},
  PlotLegends -> Placed[{"Single Moment", "Lognormal Moment Distribution"}, {0.25, 0.75}],
  AxesLabel -> {"Applied Field (Oe)", "Moment (emu)"},
  Frame -> True]

```



As can be seen in the graph above, the Lognormal Moment Distribution model (in purple) matches the data (the blue dots) better than the Single Moment model (the dashed black curve). The Single Moment model gives a slightly higher magnetic moment of 3.17×10^{-15} emu versus the Lognormal Moment Distribution model, which gives a median magnetic moment of 3.37×10^{-15} emu and a σ value of 1.9.

Appendix B

Solidworks CAD Designs

Figures of the CAD designs of the aluminum channel base, toluene-compatible glass plate, and plexiglass plate used during the experimental section of this thesis have been included in this Appendix.

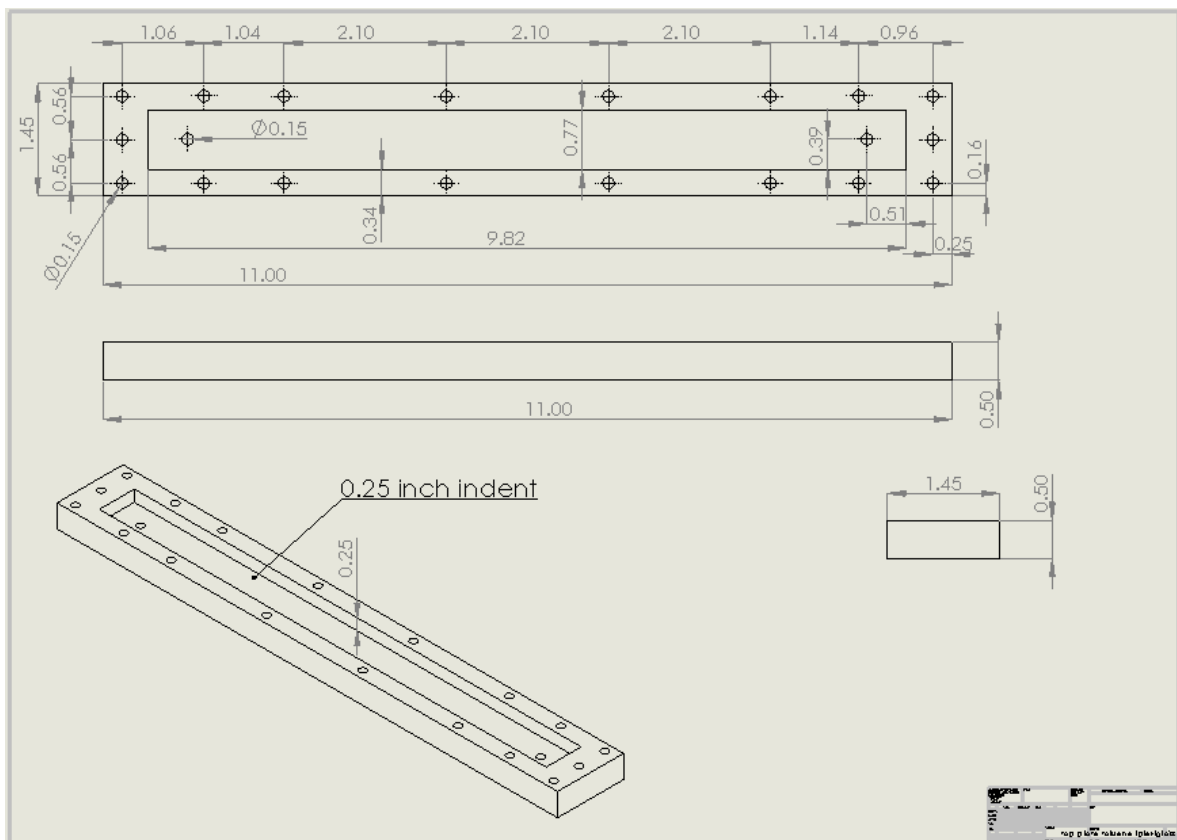


Figure B.1: Design of the plexiglass top for the toluene-compatible channel, designed by Emily Hamlin, with holes for 18 aluminum screws to hold the system tight and prevent leaks of nanoparticle solutions.

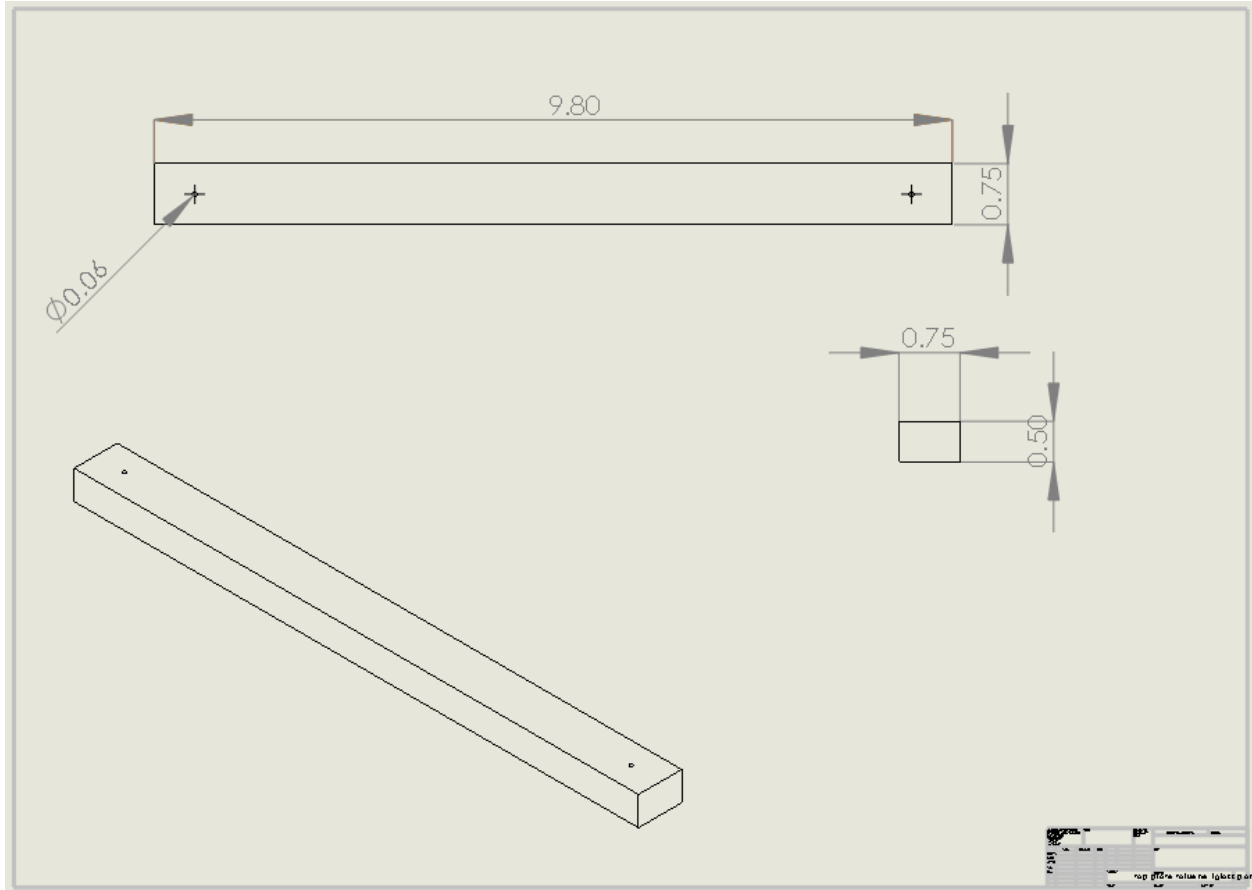


Figure B.2: Design of the glass component for the toluene-compatible channel, designed by Emily Hamlin, with two holes for plastic tubing. This piece was held in place by the plexiglass piece shown in Figure B.1.

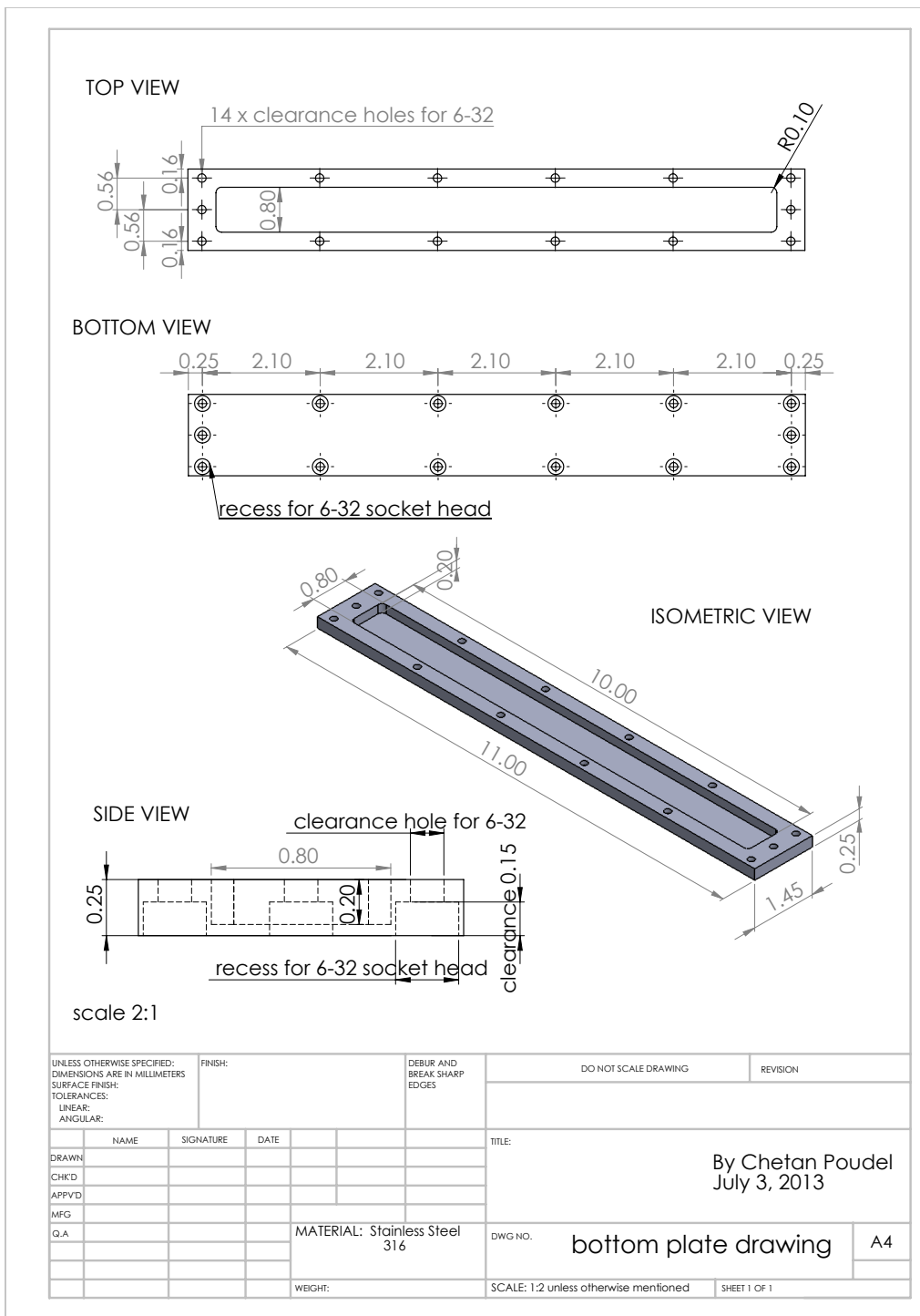


Figure B.3: Design of the stainless steel bottom plate used in the toluene-compatible channel, designed by Chetan Poudel in such a way that the glass plate fits tightly. Screws hold the bottom plate with the top plate and hold the glass plate in the middle firmly in place.